An Anelastic Allspeed Projection Method for Gravitationally Stratified Flows

Caroline Gatti-Bono and Phillip Colella

Lawrence Berkeley National Laboratory, Berkeley, CA

Abstract

This paper looks at gravitationally-stratified atmospheric flows at low Mach and Froude numbers and proposes a new algorithm to solve the compressible Euler equations, in which the asymptotic limits are recovered numerically and the boundary conditions for block-structured local refinement methods are well-posed.

The model is non-hydrostatic and the numerical algorithm uses a splitting to separate the fast acoustic dynamics from the slower anelastic dynamics. The acoustic waves are treated implicitly while the anelastic dynamics is treated semi-implicitly and an embedded-boundary method is used to represent mountain ranges. We present an example that verifies our asymptotic analysis and a set of results that compares very well with the classical gravity wave results presented by Durran.

Key words:
Non-hydrostatic atmospheric model, embedded-boundary method, projection method, gravity waves

Introduction

Gravitationally stratified flows in a compressible medium at low Mach and Froude numbers arise in atmospheric fluid dynamics or in the modeling of stars. Traditionally, such flows have been simulated either by solving the fully compressible equations or by the use of hydrostatic or anelastic models. Each

Email address: pcolella@lbl.gov (Caroline Gatti-Bono and Phillip Colella).

[1] Supported at the Lawrence Berkeley National Laboratory by the U.S Department of Energy: Director, Office of Science, Office of Advanced Scientific Computing, Mathematical, Information, and Computing Sciences Division under Contract DE-AC03-76SF00098.

of these formulations is desirable for particular properties in various asymptotic limits. Our goal is to obtain these various limits numerically from a discretization of the full compressible equations, depending on the scales being resolved. In addition, we seek a formulation for which the acoustic dynamics, the dynamics due to stiff gravity waves, and the advective dynamics, can be separated out and each treated with a suitable explicit or implicit method. Finally, we are looking for a formulation that admits well-posed general boundary-value problems. The latter property is essential for the development of block-structured local refinement methods, but, for example, does not hold for hydrostatic models [25].

In this paper, we describe a new algorithm for the compressible flow equations in a thin, gravitationally stratified layer that takes us part of the way in meeting these goals. It is based on an an extension of the allspeed projection algorithm developed by Colella and Pao [9] to the case of an anelastic Hodge decomposition of the velocity field into solenoidal and potential components, along with a corresponding splitting of the pressure field. We further modify this splitting to correctly represent the dynamics of gravity waves for thin layers. This allows us to use an implicit method for treating the acoustic modes, combined with a semi-implicit method for the anelastic dynamics. We combine this method with appropriate spatial discretizations, including an embedded boundary treatment of orography. The resulting method has as a time step limitation the CFL condition for the fast gravity waves. Since the compressible flow equations have a well-posed boundary-value formulation, the overall method is well-posed. In addition, the individual PDEs that are solved in the various substeps have well-posed boundary-value formulations, thus making it a suitable starting point for an extension to locally refined meshes. Furthermore, since the splitting is of the full equations, there is a natural embedding of the thin-layer asymptotics into a more complete fundamental system of equations in multiscale calculations, in which the resolved horizontal scales become locally comparable to the vertical scales.

We test the method on two problems. The first comes from using the thin-layer asymptotics to derive linear gravity waves. We use the fully compressible algorithm described above to compute the propagation of these waves, and obtain results compatible with the asymptotic analysis. We also use the method to compute the test problems of Durran [10] for lee waves over a mountain, and obtain good agreement with the results in the literature. In the conclusions, we discuss possible approaches to eliminating the constraint on the time step due to the fast gravity waves.

1 Anelastic All-Speed Formulation

1.1 Equations

We consider a compressible inviscid fluid, described by the Euler equations

$$\frac{\partial \rho}{\partial t} + div(\rho \mathbf{u}) = 0 \tag{1}$$
$$\frac{\partial \mathbf{u}}{\partial t} + \mathbf{u} \cdot \mathbf{grad}(\mathbf{u}) + \frac{1}{\rho}\mathbf{grad}(p) + g\mathbf{k} = 0 \tag{2}$$
$$\frac{\partial p}{\partial t} + \mathbf{u} \cdot \mathbf{grad}(p) + \rho c^2 div(\mathbf{u}) = 0 \tag{3}$$

or, in perturbational form,

$$\frac{\partial \tilde{\rho}}{\partial t} + div(\tilde{\rho}\mathbf{u}) + div(\rho_o \mathbf{u}) = 0 \tag{4}$$
$$\frac{\partial \mathbf{u}}{\partial t} + \mathbf{u} \cdot \mathbf{grad}(\mathbf{u}) + \frac{1}{\rho}\mathbf{grad}(\tilde{p}) + \frac{\tilde{\rho}}{\rho} g\mathbf{k} = 0 \tag{5}$$
$$\frac{\partial \tilde{p}}{\partial t} + \mathbf{u} \cdot \mathbf{grad}(\tilde{p}) + \rho c^2 div(\mathbf{u}) - w\rho_o g = 0 \tag{6}$$

Here, $\rho_o(z)$ is the hydrostatic density, $\tilde{\rho} = \rho - \rho_o$ is the perturbational density, $p_o(z)$ is the hydrostatic pressure defined as

$$\frac{dp_o}{dz} = -\rho_o g \tag{7}$$

and $\tilde{p} = p - p_o$ is the perturbational pressure.

Equations (4)–(6) support acoustic waves and an explicit numerical discretization of these will require a time step dictated by the acoustic dynamics. However, since the acoustic waves have a negligible effect in atmospheric dynamics, using a small time step dictated by the vertical propagating acoustic waves, about 10 times smaller than the one dictated by the horizontally propagating gravity waves, is a huge performance loss. Therefore, we split the dynamics, separating the acoustic waves from the slower anelastic dynamics.

$$\mathbf{u} = \mathbf{u}_d + \mathbf{u}_p + \mathbf{u}_h \tag{8}$$
$$div(\eta_o \mathbf{u}_d) = 0 \tag{9}$$
$$div\,(\eta_o \mathbf{u}_h) = 0 \tag{10}$$
$$\mathbf{u}_p = \mathbf{grad}(\varphi) \tag{11}$$

$$\mathbf{u}_h = \mathbf{grad}(\upsilon) \tag{12}$$

where $\mathbf{u}$ is the total velocity, $\mathbf{u}_d$ is the anelastic velocity, $\mathbf{u}_p$ is the curl-free velocity and $\mathbf{u}_h$ is the harmonic velocity, and $\eta_o = \eta_o(z)$ is a function to be determined later. The velocities must also satisfy the following relationships on Neumann boundaries

$$\mathbf{u}_d \cdot \mathbf{n} = 0 \tag{13}$$
$$\mathbf{u}_p \cdot \mathbf{n} = 0 \tag{14}$$
$$\mathbf{u}_h \cdot \mathbf{n} = \mathbf{u}.\mathbf{n} \tag{15}$$

The anelastic and curl-free velocities can also be obtained from the total velocity

$$\mathbf{u}_d = \mathbb{P}_o(\mathbf{u} - \mathbf{u}_h) \tag{16}$$
$$\mathbf{u}_p = \mathbb{Q}_o(\mathbf{u} - \mathbf{u}_h) \tag{17}$$

by using projection operators defined as follows

$$\mathbb{Q}_o(\mathbf{w}) = \mathbf{grad}\left(\mathbb{L}_{\frac{1}{\eta_o}}\right)^{-1} div\left(\eta_o \mathbf{w}\right) \tag{18}$$
$$\mathbb{P}_o(\mathbf{w}) = \left(\mathbb{I} - \mathbb{Q}_o\right)(\mathbf{w}) \tag{19}$$

where $\mathbb{L}_{\frac{1}{\beta}}\varphi = div\left(\beta \mathbf{grad}\varphi\right)$. The boundary conditions will be discussed later.

Using the splitting, equations (4)–(6) can be rewritten

$$\frac{\partial \tilde{\rho}}{\partial t} + \rho_o w\left[\frac{1}{\rho_o}\frac{d\rho_o}{dz} - \frac{1}{\eta_o}\frac{d\eta_o}{dz}\right] + div(\tilde{\rho}\mathbf{u}) + \frac{\rho_o}{\eta_o} div(\eta_o \mathbf{u}_p) = 0 \tag{20}$$

$$\frac{\partial \mathbf{u}_d}{\partial t} + \mathbf{A}_d\mathbf{u} + \frac{1}{\rho}\mathbf{grad}(\pi_I) + \frac{1}{\rho}\frac{\partial \pi_H}{\partial x}\mathbf{i} + \frac{1}{\rho}\mathbf{grad}(\psi) + \mathbb{P}_o\left[\frac{1}{\rho}\mathbf{grad}\delta + \mathbf{grad}\frac{|\mathbf{u}_p + \mathbf{u}_h|^2}{2}\right] = 0 \tag{21}$$

$$\frac{\partial \mathbf{u}_p}{\partial t} + \mathbb{Q}_o\left[\frac{1}{\rho}\mathbf{grad}\delta + \mathbf{grad}\frac{|\mathbf{u}_p + \mathbf{u}_h|^2}{2}\right] = 0 \tag{22}$$

$$\frac{\partial \delta}{\partial t} + \frac{\partial \pi_H}{\partial t} + \frac{\partial \pi_I}{\partial t} + \frac{\partial \psi}{\partial t} + \mathbf{u}\cdot\mathbf{grad}(\pi_I + \pi_H + \delta + \psi) + \frac{\rho c^2}{\eta_o} div(\eta_o \mathbf{u}_p) - w\left[\frac{\rho c^2}{\eta_o}\frac{d\eta_o}{dz} + \rho_o g\right] = 0 \tag{23}$$

where the following quantities have been introduced

- $\mathbf{A_d u}$ is the advective term defined as

$$\mathbf{A_d u} = (\mathbf{u} \cdot \mathbf{grad})\,\mathbf{u} - \mathbf{grad}\left(\frac{|\mathbf{u_p} + \mathbf{u_h}|^2}{2}\right) \tag{24}$$

- π_H and π_I are defined as

$$\frac{\partial \pi_H}{\partial z} = -\tilde{\rho} g \tag{25}$$

$$\frac{1}{\rho}\Big(\mathbf{grad}\pi_I\Big) = -\mathbb{Q}_\rho\left(\mathbf{A_d u}\right) \tag{26}$$

with

$$\mathbb{Q}_\rho \mathbf{w} = \frac{1}{\rho}\mathbf{grad}\left(\mathbb{L}_{\frac{\rho}{\eta_o}}\right)^{-1} div \eta_o \mathbf{w} \tag{27}$$

- ψ is defined as

$$\frac{1}{\rho}\mathbf{grad}(\psi) = -\mathbb{Q}_\rho\left(\frac{1}{\rho}\frac{\partial \pi_H}{\partial x}\mathbf{i}\right) \tag{28}$$

- δ is the "acoustic pressure"

$$\delta = p - p_o(z) - \pi - \psi \tag{29}$$

We choose η_o to cancel the buoyancy term $\rho_o g w$ in the pressure equation.

$$\frac{1}{\eta_o}\frac{d\eta_o}{dz} = -\frac{\rho_o g}{\gamma p_o} = \frac{1}{\gamma p_o}\frac{dp_o}{dz} \qquad \eta_o(0) = \rho_o(0) \tag{30}$$

It is to be noted that η_o comes out to be the isentropic density corresponding to the pressure distribution p_o. With this value of η_o, equations (20)–(23) become

$$\frac{\partial \tilde{\rho}}{\partial t} - \frac{\rho_o N^2}{g} w + div(\tilde{\rho}\mathbf{u}) + \frac{\rho_o}{\eta_o} div(\eta_o \mathbf{u}_p) = 0 \tag{31}$$

$$\frac{\partial \mathbf{u}_d}{\partial t} + \mathbf{A}_d \mathbf{u} + \frac{1}{\rho}\mathbf{grad}(\pi_I) + \frac{1}{\rho}\frac{\partial \pi_H}{\partial x}\mathbf{i} + \frac{1}{\rho}\mathbf{grad}(\psi) + \mathbb{P}_o\left[\frac{1}{\rho}\mathbf{grad}\delta + \mathbf{grad}\frac{|\mathbf{u}_p + \mathbf{u}_h|^2}{2}\right] = 0 \tag{32}$$

$$\frac{\partial \mathbf{u}_p}{\partial t} + \mathbb{Q}_o\left[\frac{1}{\rho}\mathbf{grad}\delta + \mathbf{grad}\frac{|\mathbf{u}_p + \mathbf{u}_h|^2}{2}\right] = 0 \tag{33}$$

$$\frac{\partial \delta}{\partial t} + \frac{\partial \pi_H}{\partial t} + \frac{\partial \pi_I}{\partial t} + \frac{\partial \psi}{\partial t} + \mathbf{u} \cdot \mathbf{grad}(\pi_I + \pi_H + \delta + \psi)$$

$$+\frac{\rho c^2}{\eta_o} div(\eta_o \mathbf{u}_p) + (\pi_I + \pi_H + \delta + \psi)\frac{\rho_o g w}{p_o} = 0 \tag{34}$$

where N is the Brunt-Väisälä frequency defined by

$$\frac{N^2}{g} = \frac{1}{\eta_o}\frac{d\eta_o}{dz} - \frac{1}{\rho_o}\frac{d\rho_o}{dz} \tag{35}$$

1.2 Asymptotic Analysis

We use asymptotics to analyze the extent to which we have decoupled buoyancy effects from compressive motions. We use tools similar to Klein's [18] but our ultimate goal is different since we want to organize the full equations in a way that reflects the asymptotics and not to use the asymptotic equations as part of our numerical scheme for specific limits.

We start by linearizing equations (31)–(34) around the state $\tilde{\rho} = 0$ and $(u, w) = 0$

$$\frac{\partial \tilde{\rho}}{\partial t} - \rho_o \frac{N^2}{g} w + \frac{\rho_o}{\eta_o} div(\eta_o \mathbf{u}_p) = 0 \tag{36}$$

$$\frac{\partial \mathbf{u}_d}{\partial t} + \frac{1}{\rho_o}\frac{\partial \pi_H}{\partial x}\mathbf{i} + \frac{1}{\rho_o}\mathbf{grad}(\psi) + \mathbb{P}_o\left[\frac{1}{\rho_o}\mathbf{grad}\delta\right] = 0 \tag{37}$$

$$\frac{\partial \mathbf{u}_p}{\partial t} + \mathbb{Q}_o\left[\frac{1}{\rho_o}\mathbf{grad}\delta\right] = 0 \tag{38}$$

$$\frac{\partial \delta}{\partial t} + \frac{\partial \pi_H}{\partial t} + \frac{\partial \psi}{\partial t} + \frac{\rho_o c_o^2}{\eta_o} div(\eta_o \mathbf{u}_p) = 0 \tag{39}$$

If U is the horizontal velocity scale, $\bar{c}$ is the average speed of sound, Λ is the speed of a typical gravity wave, l_v is the vertical length scale, L is the horizontal length scale, $\bar{N}$ is the average Brunt-Väisälä and g is the gravity constant, we can introduce the following dimensionless variables

$$\hat{x} = \frac{x}{L} \tag{40}$$

$$\varepsilon = \frac{l_v}{L} \tag{41}$$

$$\hat{z} = \frac{z}{\varepsilon L} \tag{42}$$

$$\Lambda = \sqrt{\varepsilon L g} = \varepsilon L \bar{N} \tag{43}$$

$$\hat{t} = \frac{\Lambda}{L} t \tag{44}$$

$$\hat{u} = \frac{u}{U} \tag{45}$$
$$\hat{w} = \frac{w}{W} \tag{46}$$
$$\hat{u_d} = \frac{u_d}{U_d} \tag{47}$$
$$\hat{w_d} = \frac{w_d}{W_d} \tag{48}$$
$$\hat{u_p} = \frac{u_p}{U_p} \tag{49}$$
$$\hat{w_p} = \frac{w_p}{W_p} \tag{50}$$
$$\mathcal{F}r = \frac{U}{\Lambda} \tag{51}$$
$$\mathcal{M} = \frac{U}{\bar{c}} \tag{52}$$

where $\mathcal{M}$ is the Mach number, ε is the aspect ratio and $\mathcal{F}r$ is the Froude number. Our choice of time scale reflects the fact that the fast gravity waves are of interest in this study.

For mesoscale atmospheric flows, we have the following relationships between the different parameters defined above

$$\varepsilon \ll 1 \tag{53}$$
$$\mathcal{M} \sim \mathcal{F}r \ll 1 \tag{54}$$
$$W_d = \varepsilon U_d \tag{55}$$

Using equation (11), we obtain

$$W_p = \frac{U_p}{\varepsilon} \tag{56}$$

These parameters are used to estimate the magnitude of the different contributions to the pressure π_H, ψ and δ (π_I depends quadratically on $\mathbf{u}$ and is therefore negligible in the present analysis). Using equations (36), (37) and (38) along with the definitions of π_H and ψ, multiplying by η_o and applying the divergence operator, we obtain

$$\begin{aligned}\frac{\bar{\rho}\Lambda U_p}{L^2}\left(\frac{\partial}{\partial\hat{x}}\left(\hat{\eta_o}\frac{\partial\hat{u}_p}{\partial\hat{t}}\right)+\frac{1}{\varepsilon^2}\frac{\partial}{\partial\hat{z}}\left(\hat{\eta_o}\frac{\partial\hat{w}_p}{\partial\hat{t}}\right)\right)\\ +\frac{1}{L^2}\left(\frac{\partial}{\partial\hat{x}}\left(\frac{\hat{\eta}_o}{\hat{\rho}_o}\frac{\partial\delta}{\partial\hat{x}}\right)+\frac{1}{\varepsilon^2}\frac{\partial}{\partial\hat{z}}\left(\frac{\hat{\eta}_o}{\hat{\rho}_o}\frac{\partial\delta}{\partial\hat{z}}\right)\right)=0\end{aligned} \tag{57}$$

$$\frac{\partial}{\partial \hat{z}}\left(\frac{\partial \pi_H}{\partial \hat{t}}\right) = -\bar{\rho}\Lambda U \hat{\rho}_o \hat{N}^2 \hat{w} + \bar{\rho}\Lambda U_p \frac{\hat{\rho}_o}{\hat{\eta}_o}\left(\frac{\partial \hat{\eta}_o \hat{u}_p}{\partial \hat{x}} + \frac{1}{\varepsilon^2}\frac{\partial \hat{\eta}_o \hat{w}_p}{\partial \hat{z}}\right) \tag{58}$$

$$\frac{\bar{\rho}\Lambda U_d}{L^2}\left(\frac{\partial}{\partial \hat{x}}\left(\hat{\eta_o}\frac{\partial \hat{u}_d}{\partial \hat{t}}\right) + \frac{\partial}{\partial \hat{z}}\left(\hat{\eta_o}\frac{\partial \hat{w}_d}{\partial \hat{t}}\right)\right)$$
$$+\frac{1}{L^2}\left(\frac{\hat{\eta_o}}{\hat{\rho_o}}\frac{\partial^2 \pi_H}{\partial \hat{x}^2} + \frac{\hat{\eta_o}}{\hat{\rho_o}}\frac{\partial^2 \psi}{\partial \hat{x}^2} + \frac{1}{\varepsilon^2}\frac{\partial}{\partial \hat{z}}\left(\frac{\hat{\eta_o}}{\hat{\rho_o}}\frac{\partial \psi}{\partial \hat{z}}\right)\right) = 0 \tag{59}$$

$$\frac{1}{L^2}\frac{\partial}{\partial \hat{x}}\left(\frac{\hat{\eta}_o}{\hat{\rho}_o}\frac{\partial \psi}{\partial \hat{x}}\right) + \frac{1}{\varepsilon^2 L^2}\frac{\partial}{\partial \hat{z}}\left(\frac{\hat{\eta}_o}{\hat{\rho}_o}\frac{\partial \psi}{\partial \hat{z}}\right) = -\frac{1}{L^2}\frac{\partial}{\partial \hat{x}}\left(\frac{\hat{\eta}_o}{\hat{\rho}_o}\frac{\partial \pi_H}{\partial \hat{x}}\right) \tag{60}$$

$$U\hat{u} = U_d \hat{u}_d + U_p \hat{u}_p \tag{61}$$

This gives us the following estimates of the magnitude for the velocities and the various pressure terms.

$$U_p = O\left(\varepsilon^2 U_d\right) \tag{62}$$
$$U_d = O(U) \tag{63}$$
$$\pi_H = O\left(\bar{\rho}\Lambda U\right) \tag{64}$$
$$\delta,\, \psi = O\left(\varepsilon^2 \bar{\rho}\Lambda U\right) \tag{65}$$

From this it follows that (39) reduces to

$$\frac{1}{\rho_o c_o^2}\frac{\partial \pi_H}{\partial t} + \frac{1}{\eta_o} div(\eta_o \mathbf{u}_p) = O\left(\varepsilon^2 \frac{U}{L}\right) \tag{66}$$

Each term in the left-hand side is individually $O\left(\frac{U}{L}\right)$.

We note now that the velocities satisfy the following relationships

$$u_d = O(U) \tag{67}$$
$$u_p = O\left(\varepsilon^2 U\right) \tag{68}$$
$$w_d = O\left(\varepsilon U\right) \tag{69}$$
$$w_p = O\left(\varepsilon U\right) \tag{70}$$

Therefore, w_d and w_p are of comparable magnitude and w_p must be included in the equations to account for the complete vertical dynamics. In the pseudo-incompressible approximation [11], the divergence-free constraint is applied to the total velocity

$$div(\eta_o \mathbf{u}) = 0 \tag{71}$$

which is equivalent to discarding the potential velocity $\mathbf{u}_p$, which leads to advective dynamics different from the present approach.

Also, we recover the classical assumption

$$W = \varepsilon U \tag{72}$$

i.e. that the horizontal and vertical advective time scales are comparable.

Equation (66) is used to derive a system of hyperbolic equations (as shown in the Appendix)

$$\mathcal{L}_z \frac{\partial \pi_H}{\partial t} + \eta_o \frac{\partial u_d}{\partial x} = O(\varepsilon^2) \tag{73}$$

$$\frac{\partial u_d}{\partial t} + \frac{1}{\rho_o} \frac{\partial \pi_H}{\partial x} = O(\varepsilon^2) \tag{74}$$

where

$$\mathcal{L}_z = -\frac{\partial}{\partial z}\left[\frac{\eta_o g}{\rho_o N^2}\left(\frac{1}{g}\frac{\partial}{\partial z} + \frac{1}{c_o^2}\right)\right] + \frac{\eta_o}{\rho_o c_o^2} \tag{75}$$

The operator $\mathcal{L}_z$ can be rewritten in the form

$$\mathcal{L}_z = -\frac{\partial}{\partial z}\left[\frac{\eta_o g}{\rho_o N^2}\left(\frac{1}{g}\frac{\partial}{\partial z} + \frac{1}{c_o^2}\right)\right] + \frac{\eta_o}{\rho_o c_o^2} = -\xi\left[\frac{\partial}{\partial z}\zeta\frac{\partial}{\partial z} + \chi\right] \tag{76}$$

with

$$\xi = exp\left(-\int_o^z \frac{g}{c_o^2} dz\right) \tag{77}$$

$$\zeta = \frac{\eta_o}{\rho_o N^2} exp\left(\int_o^z \frac{g}{c_o^2} dz\right) \tag{78}$$

$$\chi = \frac{\eta_o}{\rho_o c_o^2}\left[(\gamma - 1)\frac{g^2}{N^2 c_o^2} - 1\right] exp\left(\int_o^z \frac{g}{c_o^2} dz\right) \tag{79}$$

When χ is negative, the operator is positive definite and equations (73)–(74) describe the motion of an infinite collection of horizontally propagating gravity

waves, one for each eigenmode of the second-order self-adjoint operator $\mathcal{L}_z$. When χ is positive, the first few eigenvalues can become negative, as shown in Figure 1, and this is a direct consequence of including the potential dynamics into the asymptotic analysis. We observe that this has a stabilizing effect as the modes with negative eigenvalues do not support gravity waves.

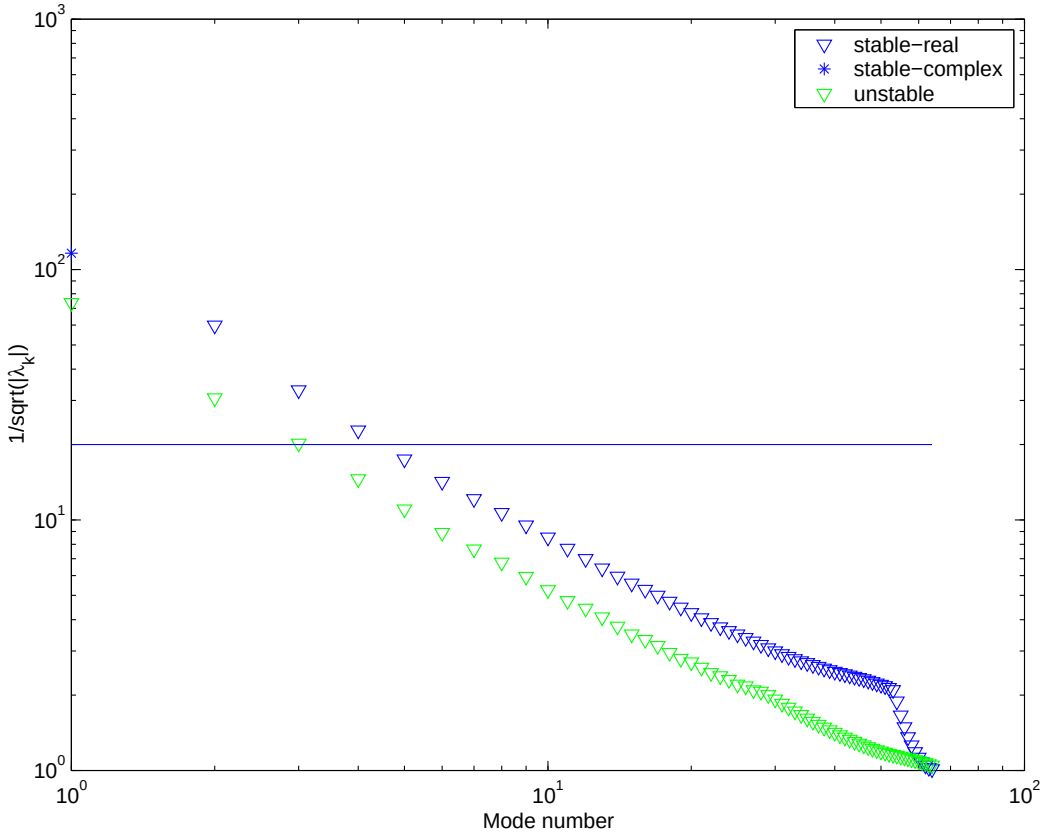

Fig. 1. "Speed" of gravity waves for the quarter-wavelength stable and unstable cases shown in the results section.

The asymptotic analysis is similar to the normal mode analysis presented by Baer and Tribbia [3], Tribbia [31], Temperton and Williamson ([30] and [32]), but we use the full compressible PDEs instead of the discretized version of the hydrostatic equations. The eigenvalues λ^k are real and the (normalized) eigenvectors r^k form an orthonormal basis in L^2. The speeds of the gravity waves are then given by

$$c^k = \frac{1}{\sqrt{\lambda^k}} \tag{80}$$

and are shown on Figure 2 for an example presented in the results section. This figure shows that the gravity waves for only a few modes travel faster than a typical fluid velocity for large-scale motions of $20\,m/s$ (marked in a

solid line on the graph). If these modes were isolated and treated implicitly, then we could use a CFL condition based only on the speed of the fluid, which could lead to a considerable gain in computational efficiency.

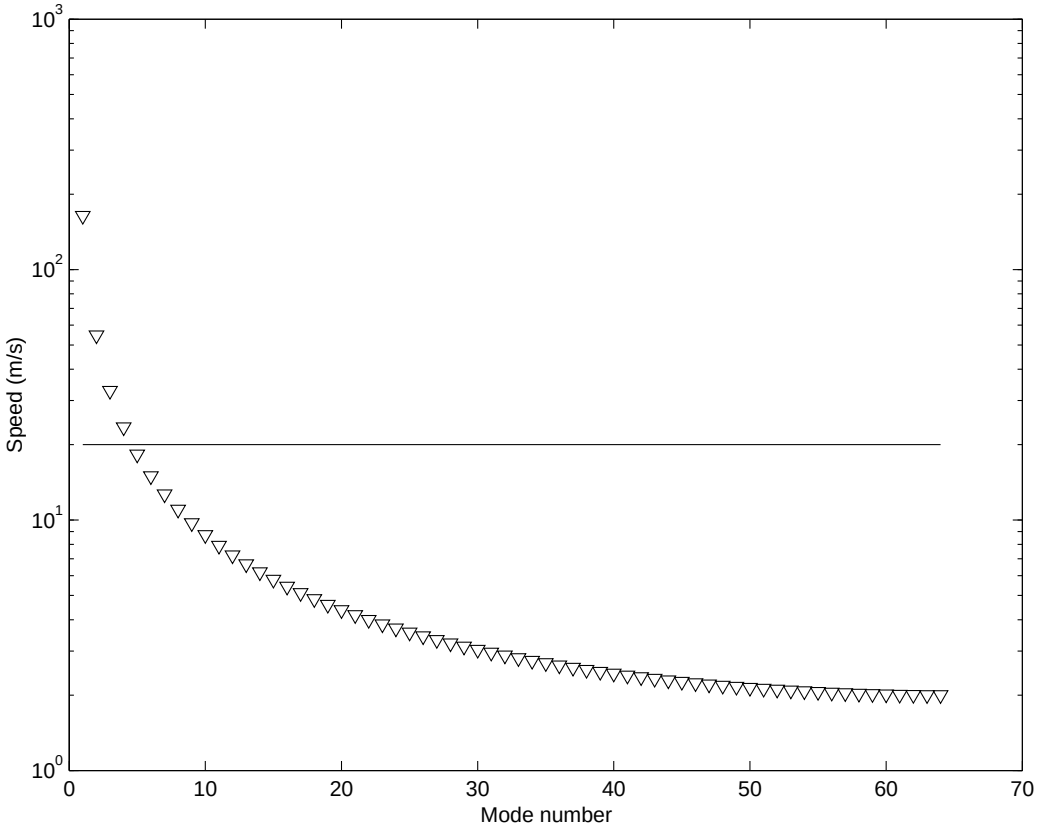

Fig. 2. Speed of gravity waves for the perturbational gravity-wave test problem of section 4.

2 Time Discretization

In this section, we will introduce the quantities that are solved for and we will present only the time discretization that is used to advance the solution. We made the choice to dissociate time and spatial discretizations for clarity purposes. The time discretization of the equations (31)–(34) gives the blueprint of the numerical algorithm that should not be overshadowed by the technicalities of spatial discretizations and centerings, which can be found in the subsequent section 3.

2.1 Variables and Time Discretization

Time is discretized using Δt. The variables that we solve for are the total velocity $\mathbf{u} = (u, w)$, the anelastic velocity $\mathbf{u}_d = (u_d, w_d)$, the curl-free velocity $\mathbf{u}_p = (u_p, w_p)$, the total pressure p, the acoustic pressure δ, the auxiliary pressures ψ, π_H and π_I, the density ρ, and the perturbational density $\tilde{\rho}$.

2.2 Time Discretization of Equations (31)–(34)

The system (31)–(34) is discretized in time using a combination of explicit or implicit schemes. First, a few quantities are partially advanced, considering only the advective dynamics, so that the auxiliary pressure π_I can be advanced to half time step in order to compute the acoustic pressure. Then, the curl-free velocity is advanced and the quantities that were partially or temporarily advanced are corrected.

- First, the anelastic velocity is partially advanced in time using only the advection terms in equation (32)

$$\mathbf{u}_d^* = \mathbf{u}_d^n - \Delta t \left(\left(\mathbf{A_d u} \right)^{n+\frac{1}{2}} \right) \tag{81}$$

- Then, we use equation (31) to temporarily advance the density variables ρ and $\tilde{\rho}$

$$\tilde{\rho}^{n+1} = \tilde{\rho}^n + \Delta t \left(\frac{\partial \tilde{\rho}}{\partial t} \right)^{n+\frac{1}{2}} \tag{82}$$

$$\rho^{n+1} = \tilde{\rho}^{n+1} + \rho_o \tag{83}$$

$$\rho^{n+\frac{1}{2}} = \frac{\rho^{n+1} + \rho^n}{2} \tag{84}$$

- Equation (25) is used to temporarily advance π_H

$$\pi_H^{n+1} = \int_z^L \tilde{\rho}^{n+1} g d\check{z} \qquad \left(\pi_H(L) = 0 \right) \tag{85}$$

- Using equation (26), we solve for $\pi_I^{n+\frac{1}{2}}$

$$\frac{1}{\rho^{n+\frac{1}{2}}} \mathbf{grad} \left(\pi_I^{n+\frac{1}{2}} \right) = -\mathbb{Q}_{\rho^{n+\frac{1}{2}}} \left(\mathbf{A_d u}^{n+\frac{1}{2}} \right) \tag{86}$$

- Using equation (28), we solve for ψ^{n+1}

$$\mathbb{L}_{\frac{\rho^{n+1}}{\eta_o}}(\psi^{n+1}) = -div\left(\frac{\eta_o}{\rho^{n+1}}\frac{\partial \pi_H^{n+1}}{\partial x}\mathbf{i}\right) \tag{87}$$

- Combining equations (33) and (34), we implicitly advance the acoustic pressure

$$\begin{aligned}\mathbb{H}\delta^{n+1} \equiv & \left(\mathbb{I} - \Delta t^2 \frac{\gamma p^n}{\eta_o}\mathbb{L}_{\frac{\rho^{n+\frac{1}{2}}}{\eta_o}}\right)\delta^{n+1} \\ & = \delta^n - \Delta t\left[\frac{\gamma p^n}{\eta_o}\left\{div(\eta_o \mathbf{u}_p^n) - \Delta t div \eta_o \mathbf{grad}\left(\frac{|\mathbf{u}_p^n + \mathbf{u}_h|^2}{2}\right)\right\}\right. \\ & \left. + \mathbf{u}^{n+\frac{1}{2}} \cdot (\mathbf{grad}\,(\delta^n + \pi^n + \psi^n)) - w^{n+\frac{1}{2}}\left[\frac{\rho^n c^{n2}}{\eta_o}\frac{d\eta_o}{dz} + \rho_o g\right]\right] \\ & - \left(\pi_I^{n+\frac{1}{2}} + \pi_H^{n+1} + \psi^{n+1} - \pi_I^{n-\frac{1}{2}} - \pi_H^n - \psi^n\right)\end{aligned} \tag{88}$$

where

$$w^{n+\frac{1}{2}} = w_d^{n+\frac{1}{2}} + w_p^n + w_h \tag{89}$$

- Then, we advance the curl-free velocity using equation (33)

$$u_p^{n+1} = u_p^n - \Delta t \mathbb{Q}_o\left(\mathbf{grad}\left(\frac{|\mathbf{u}_p^n + \mathbf{u}_h|^2}{2}\right) + \left(\frac{1}{\rho^n}\Big(\mathbf{grad}\delta^{n+1}\Big)\right)\right) \tag{90}$$

- The perturbational density is advanced using equation (31)

$$\tilde{\rho}^{n+1} = \tilde{\rho}^n - \Delta t \frac{\rho_o N^2}{g} w^{n+\frac{1}{2}} - \Delta t \frac{\rho_o}{\eta_o} div\left(\eta_o \mathbf{u}_p^{n+1}\right) - \Delta t div(\tilde{\rho}\mathbf{u})^{n+\frac{1}{2}} \tag{91}$$

- π_H is updated

$$\pi_H^{n+1} = \int_z^L \tilde{\rho}^{n+1} g d\check{z} \qquad \Big(\pi_H(L) = 0\Big) \tag{92}$$

- ψ is updated

$$\mathbb{L}_{\frac{\rho^{n+1}}{\eta_o}}(\psi^{n+1}) = -div\left(\frac{\eta_o}{\rho^{n+1}}\frac{\partial \pi_H^{n+1}}{\partial x}\mathbf{i}\right) \tag{93}$$

- We finish advancing the divergence-free velocity

$$u_d^{n+1} = u_d^* - \Delta t \left(\frac{1}{\rho^{n+\frac{1}{2}}} \left(\mathbf{grad} \pi_I^{n+\frac{1}{2}} \right) + \frac{1}{\rho^{n+1}} \left(\mathbf{grad} \psi^{n+1} \right) + \frac{1}{\rho^{n+1}} \frac{\partial \pi_H^{n+1}}{\partial x} \mathbf{i} \right.$$
$$\left. + \mathbb{P}^o \left(\frac{1}{\rho^n} \left(\mathbf{grad} \delta^{n+1} \right) + \mathbf{grad} \left(\frac{|\mathbf{u}_p^n + \mathbf{u}_h|^2}{2} \right) \right) \right) \tag{94}$$

2.3 Boundary conditions

2.3.1 Inflow

At an inflow boundary, the velocity field in an inviscid model must satisfy

$$\mathbf{u} \cdot \mathbf{n} = u_n \tag{95}$$

Because the splitting satisfies equations (13)–(15), we have

$$\mathbf{u}_d \cdot \mathbf{n} = 0 \tag{96}$$
$$\mathbf{u}_p \cdot \mathbf{n} = 0 \tag{97}$$
$$\mathbf{u}_h \cdot \mathbf{n} = u_n \tag{98}$$

The density is held constant at inflow

$$\rho = \rho_o \tag{99}$$
$$\tilde{\rho} = 0 \tag{100}$$

where ρ_o is the hydrostatic density distribution.

Now, we look at the more complicated boundary conditions for the projection and Helmholtz operators of equations (86)–(90). At the boundary, equation (86) becomes

$$\frac{1}{\rho^{n+\frac{1}{2}}} \frac{\partial \pi_I^{n+\frac{1}{2}}}{\partial n} = -\mathbf{n} \cdot \mathbb{Q}_{\rho^{n+\frac{1}{2}}} \left(\mathbf{A_d} \mathbf{u}^{n+\frac{1}{2}} + \frac{1}{\rho^{n+\frac{1}{2}}} \frac{\partial \pi_H^{n+\frac{1}{2}}}{\partial x} \mathbf{i} \right) \tag{101}$$

By definition of the splitting, the anelastic component must be parallel to the boundary near the boundary, as seen in equations (13)–(15), and we obtain

$$\mathbf{n} \cdot \mathbb{P}_{\rho^{n+\frac{1}{2}}} \left(\mathbf{A_d} \mathbf{u}^{n+\frac{1}{2}} + \frac{1}{\rho^{n+\frac{1}{2}}} \frac{\partial \pi_H^{n+\frac{1}{2}}}{\partial x} \mathbf{i} \right) = 0 \tag{102}$$

and therefore

$$\frac{1}{\rho^{n+\frac{1}{2}}} \frac{\partial \pi_I^{n+\frac{1}{2}}}{\partial n} = -\mathbf{n} \cdot \left(\mathbf{A_d} \mathbf{u}^{n+\frac{1}{2}} + \frac{1}{\rho^{n+\frac{1}{2}}} \frac{\partial \pi_H^{n+\frac{1}{2}}}{\partial x} \mathbf{i} \right) \tag{103}$$

Similarly, after taking the dot product of equation (90) with the normal and using condition (97), we obtain

$$\mathbf{n} \cdot \left(\mathbf{grad} \left(\frac{|\mathbf{u}_p^n + \mathbf{u}_h|^2}{2} \right) + \left(\frac{1}{\rho^n} \left(\mathbf{grad} \delta^{n+1} \right) \right) \right) = 0 \tag{104}$$

and the outflow boundary condition for the Helmholtz equation (88) becomes

$$\frac{1}{\rho^n} \frac{\partial \delta^{n+1}}{\partial n} = \mathbf{grad} \left(\frac{|\mathbf{u}_p^n + \mathbf{u}_h|^2}{2} \right) \cdot \mathbf{n} \tag{105}$$

2.3.2 Outflow

On the outflow boundary, the pressure is imposed

$$p = p_o \tag{106}$$

where p_o is the hydrostatic pressure, and this implies

$$\delta = 0 \tag{107}$$
$$\pi_I = 0 \tag{108}$$

3 Spatial Discretization

3.1 Discretizing Equations (31)–(34) on a Regular Grid

An anisotropic rectangular grid with spacing Δx and Δz is applied to the computational domain as shown in Figure 4(a). We seek the solution to the

system of equations (31)–(34) either at cell centers (i, j) or at cells faces $(i + \frac{1}{2}, j)$ or $(i, j+\frac{1}{2})$, where $i = 1 \dots N$ with N the number of cells in the horizontal direction and $j = 1 \dots M$ with M the number of cells in the vertical direction. Table 1 gives the spatial and time centering of the main variables.

	Cell-centered	Face-centered	$t^n = n\Delta t$	$t^{n+\frac{1}{2}} = \left(n + \frac{1}{2}\right) \Delta t$
(u, w)	$\surd$		$\surd$	
(u_d, w_d)	$\surd$		$\surd$	
(u_d, w_d)		$\surd$		$\surd$
(u_p, w_p)		$\surd$	$\surd$	
(u_h, w_h)		$\surd$	N/A	N/A
p	$\surd$		$\surd$	
δ	$\surd$		$\surd$	
π	$\surd$			$\surd$
π_H		$\surd$	$\surd$	
π_I	$\surd$			$\surd$
ρ	$\surd$		$\surd$	
$\tilde{\rho}$	$\surd$		$\surd$	

Table 1
Spatial and time centering of main variables

In this section, to simplify the exposition, we only look at the discretization of the different operators on regular cells, that is cells that are not cut. The discretization on cut cells will be presented in 3.2.

3.1.1 Gradient, Divergence, Laplacian and Projections

Gradient, divergence and Laplacian operators are used throughout the equations. We use different types of spatial discretizations for computing the gradient and the divergence operators depending on where the initial variables are centered and how the result must be centered.

Gradient **G**

The gradient operator **G** takes variables at cell centers and returns the gradient at cell faces.

$$\left(\mathbf{G}\varphi\right)_{x,\, i+\frac{1}{2}j} = \frac{\varphi_{i+1j} - \varphi_{ij}}{\Delta x} \tag{109}$$

On boundaries where we have a Dirichlet boundary condition $\varphi = b$, we do a linear interpolation to get

$$\Big(\mathbf{G}\varphi\Big)_{x,\,i+\frac{1}{2}j} = 2\frac{b_{i+\frac{1}{2}j} - \varphi_{ij}}{\Delta x} \tag{110}$$

When the tangential gradient needs to be computed, we use

$$\begin{aligned}\Big(\mathbf{G}\varphi\Big)_{z,\,i+\frac{1}{2}j} = \frac{1}{4}\Bigg(&\Big(\mathbf{G}\varphi\Big)_{z,\,ij+\frac{1}{2}} + \Big(\mathbf{G}\varphi\Big)_{z,\,ij-\frac{1}{2}} \\ &+\Big(\mathbf{G}\varphi\Big)_{z,\,i+1j-\frac{1}{2}} + \Big(\mathbf{G}\varphi\Big)_{z,\,i+1j-\frac{1}{2}}\Bigg)\end{aligned} \tag{111}$$

On the boundary, we extrapolate the tangential gradients to second order as shown on Figure 5.

Cell-centered Gradient $\mathbf{G}_o$

The cell-centered operator $\mathbf{G}_o$ takes variables at cell centers and returns the gradient at cell centers.

$$\mathbf{G}_o = Av^{F\to C}\mathbf{G} \tag{112}$$

where $Av^{F\to C}$ represents the following arithmetic average

$$\Big(Av^{F\to C}\left(\mathbf{G}\varphi\right)\Big)_{x,\,ij} = \frac{\left(\mathbf{G}\varphi\right)_{x,\,i-\frac{1}{2}j} + \left(\mathbf{G}\varphi\right)_{x,\,i+\frac{1}{2}j}}{2} \tag{113}$$

Face-Centered to Cell-Centered Gradient $\mathbf{G}_{F\to C}$

The gradient $\mathbf{G}_{F\to C}$ takes variables at cell faces and returns the gradient at cell centers.

$$\Big(\mathbf{G}_{F\to C}\varphi\Big)_{x,\,ij} = \frac{\varphi_{i+\frac{1}{2}j} - \varphi_{i-\frac{1}{2}j}}{\Delta x} \tag{114}$$

Divergence D

The divergence D takes a vector variable $\mathbf{w} = (u, v)$ at cell faces and returns the divergence at cell centers.

$$D\mathbf{w}_{ij} = \frac{u_{i+\frac{1}{2}j} - u_{i-\frac{1}{2}j}}{\Delta x} + \frac{v_{ij+\frac{1}{2}} - v_{ij-\frac{1}{2}}}{\Delta z} \tag{115}$$

Cell-Centered Divergence D_o

The cell-centered divergence takes a vector variable at cell centers and returns the gradient at cell centers.

$$D_o = DAv^{C\to F} \tag{116}$$

where $Av^{C\to F}$ represents the following arithmetic average

$$\left(Av^{C\to F}u\right)_{i+\frac{1}{2}j} = \frac{u_{ij}+u_{i+1j}}{2} \tag{117}$$

Operator $\mathbb{L}_\rho$

The operator $\mathbb{L}_\rho$ is given by

$$\mathbb{L}_\rho = D\frac{1}{\rho}\mathbf{G} \tag{118}$$

Projections

The discretized projections are given by:

$$\mathbb{Q}_\rho = \frac{1}{\rho}\mathbf{G}\mathbb{L}^{-1}_{\frac{\rho}{\eta_o}}D\eta_o \tag{119}$$
$$\mathbb{P}_\rho = \mathbb{I} - \mathbb{Q}_\rho \tag{120}$$
$$\mathbb{Q}^o_\rho = \frac{1}{\rho}\mathbf{G}_o\mathbb{L}^{-1}_{\frac{\rho}{\eta_o}}D_o\eta_o \tag{121}$$
$$\mathbb{P}^o_\rho = \mathbb{I} - \mathbb{Q}^o_\rho \tag{122}$$

To compute $\mathbb{Q}_\rho(\mathbf{w})$, for example, we introduce $\tilde{\mathbf{w}} = D(\eta_o\mathbf{w})$, and solve for φ

$$\mathbb{L}^H_{\frac{\rho}{\eta_o}}\varphi = \tilde{\mathbf{w}} \tag{123}$$

where $\mathbb{L}^H_{\frac{1}{\eta_o}} = D\eta_o G$ is a Poisson operator with homogeneous boundary conditions and D^{PROJ} is the divergence D where the boundary conditions are assumed to be homogeneous on Neumann boundaries. Then, we find $\mathbb{Q}_\rho(\mathbf{w})$ by

$$\mathbb{Q}_\rho\mathbf{w} = \frac{1}{\rho}\mathbf{G}\varphi \tag{124}$$

3.1.2 Advective Terms in the Anelastic Equations (31) and(32)

The operators presented above will now be used to compute the two advective terms in equations (31) and (32). $\mathbf{A_d u}$ can be written in following form

$$\begin{aligned}\mathbf{A_d u} = & \, div(\mathbf{u} \otimes \mathbf{u}_d) + div(\mathbf{u}_d \otimes (\mathbf{u}_p + \mathbf{u}_h)) \\ & -\mathbf{u}_d \cdot div(\mathbf{u}) - (\mathbf{u}_p + \mathbf{u}_h) \cdot div(\mathbf{u}_d)\end{aligned} \tag{125}$$

All derivatives are made exclusively of divergence operators and need to be evaluated at half time steps. To retain the conservation of mass property, we choose the divergence D for discretizing these two terms and, therefore, we need to get $\mathbf{u}_d$, $\mathbf{u}$ and $\tilde{\rho}$ at face centers and at half time step.

Godunov Advection Procedure

In the Godunov advection procedure, we obtain the values at face centers and half time step by first extrapolating separately from the centers of the two adjacent cells using a Taylor series expansion

$$\tilde{\rho}^{n+\frac{1}{2}}_{ij,\pm,s} = \tilde{\rho}^{n}_{ij} \pm \frac{\Delta x_s}{2}\left(\frac{\partial \tilde{\rho}}{\partial x_s}\right)^n_{ij} + \frac{\Delta t}{2}\left(\frac{\partial \tilde{\rho}}{\partial t}\right)^n_{ij} \tag{126}$$

$$\mathbf{u}^{n+\frac{1}{2}}_{d,ij,\pm,s} = \mathbf{u}^{n}_{d,ij} \pm \frac{\Delta x_s}{2}\left(\frac{\partial \mathbf{u}_d}{\partial x_s}\right)^n_{ij} + \frac{\Delta t}{2}\left(\frac{\partial \mathbf{u}_d}{\partial t}\right)^n_{ij} \tag{127}$$

where the notation is illustrated in Figure 3.

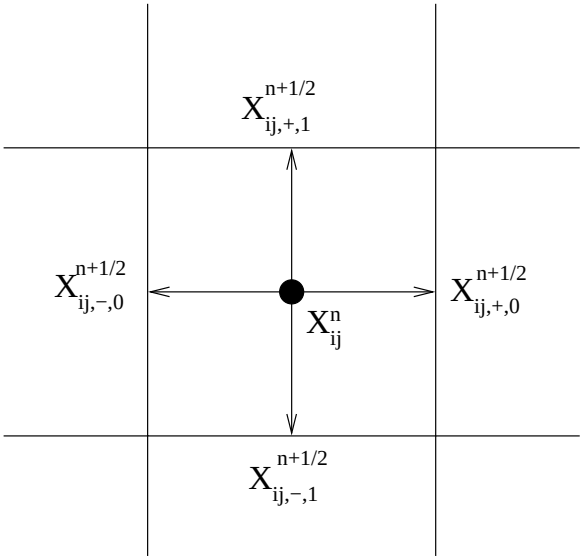

Fig. 3. Notation.

By replacing the time derivatives using either equation (31) or (32)

$$\left(\tilde{\rho}_{ij,\pm,s}^{n+\frac{1}{2}}\right) = \tilde{\rho}_{ij}^{n} \pm \frac{1}{2}\min\left\{\left(1 \mp \frac{\Delta t}{\Delta x_s}u_{ij}^{n}\right),1\right\}(\Delta_{x_s}\tilde{\rho})_{ij}^{n} - \frac{\Delta t}{2\Delta x_{s'}}w_{ij}^{n}[\tilde{\rho}]_{x_{s'},ij}^{n} - \frac{\Delta t}{2}\tilde{\rho}_{ij}^{n}\left(D_o\left(\mathbf{u}^{n}\right)\right)_{ij} - \frac{\Delta t}{2\eta_{o,ij}}\rho_{o,ij}\left(D\left(\eta_o\mathbf{u}_p^{n}\right)\right)_{ij} + \frac{\Delta t}{2}\frac{N^2\rho_{o,ij}}{g}w_{ij}^{n} \tag{128}$$

$$\left(u_{d,ij,\pm,s}^{n+\frac{1}{2}}\right) = u_{d,ij}^{n} \pm \frac{1}{2}\min\left\{\left(1 \mp u_{ij}\frac{\Delta t}{\Delta x_s}\right),1\right\}(\Delta_{x_s}u_d)_{ij}^{n} - \frac{\Delta t}{2\Delta x_{s'}}w_{ij}[u_d]_{x_{s'}\,ij}^{n} - \frac{\Delta t}{2}\left(\mathbf{u}_{d,ij}^{n}\right)_{x_s}(\mathbf{G}_{F\to C}\mathbf{u}_{pot}^{n})_{x_s,ij} - \frac{\Delta t}{2\rho_{ij}^{n}}\left(\frac{\partial\pi_H^{n}}{\partial x}\right)_{ij} - \frac{\Delta t}{2\rho_{ij}^{n}}\left(\frac{\partial\pi_I^{n}}{\partial x}\right)_{ij} - \frac{\Delta t}{2}\mathbb{P}_o^{o}\left(\frac{1}{\rho^{n}}\mathbf{G}_o(\delta^{n}) + \mathbf{G}_o\left(\frac{|\mathbf{u}_p^{n}+\mathbf{u}_h|^2}{2}\right)\right)_{x_s,ij}^{n} \tag{129}$$

where $s \neq s^{'}$ and w_{ij}^{n} is given by

$$w_{ij}^{n} = \left(w_{d,ij}^{n} + \left(Av^{F\to C}(w_p^{n})\right)_{ij}\right) \tag{130}$$

and the slopes are computed

- in the normal direction using

$$(\Delta_x u)_{ij}^{n} = \frac{u_{i+1j}^{n} - u_{i-1j}^{n}}{2}\ ; \quad (\Delta_x\tilde{\rho})_{ij}^{n} = \frac{\tilde{\rho}_{i+1j}^{n} - \tilde{\rho}_{i-1j}^{n}}{2} \tag{131}$$

- in the tangential direction using

$$[u]_{ij}^{n} = u_{ij}^{n} - u_{ij-1}^{n}\ ; \quad [\tilde{\rho}]_{ij}^{n} = \tilde{\rho}_{ij}^{n} - \tilde{\rho}_{ij-1}^{n}\,\text{if}\,w_{ij} > 0 \tag{132}$$

$$[u]_{ij}^{n} = u_{ij+1}^{n} - u_{ij}^{n}\ ; \quad [\tilde{\rho}]_{ij}^{n} = \tilde{\rho}_{ij+1}^{n} - \tilde{\rho}_{ij}^{n}\,\text{if}\,w_{ij} < 0 \tag{133}$$

Then, the solution is upwinded to get the final value of the variables on face edges

$$u_{d,\,i+\frac{1}{2}j}^{n+\frac{1}{2}}\ ;\ \tilde{\rho}_{i+\frac{1}{2}j}^{n+\frac{1}{2}} = \begin{cases} u_{d,\,ij,+,0}^{n+\frac{1}{2}}\ ;\ \tilde{\rho}_{ij,+,0}^{n+\frac{1}{2}} & \text{if}\ \ u_{i+\frac{1}{2}j}^{edge} > 0 \\ u_{d,\,i+1j,-,0}^{n+\frac{1}{2}}\ ;\ \tilde{\rho}_{i+1j,-,0}^{n+\frac{1}{2}} & \text{if}\ \ u_{i+\frac{1}{2}j}^{edge} < 0 \\ \frac{1}{2}\left(u_{d,\,ij,+,0}^{n+\frac{1}{2}} + u_{d,\,i+1j,-,0}^{n+\frac{1}{2}}\right)\ ;\ \frac{1}{2}\left(\tilde{\rho}_{ij,+,0}^{n+\frac{1}{2}} + \tilde{\rho}_{i+1j,-,0}^{n+\frac{1}{2}}\right) & \text{if}\ \ u_{i+\frac{1}{2}j}^{edge} = 0 \end{cases} \tag{134}$$

Because the new anelastic velocity does not satisfy equation (9), we introduce

a potential φ that verifies

$$\mathbb{L}_{\frac{1}{\eta_o}}\varphi = D\left(\eta_o \mathbf{u}_d^{n+\frac{1}{2}}\right) \tag{135}$$

and we correct $\mathbf{u}_d^{n+\frac{1}{2}}$

$$\mathbf{u}_d^{n+\frac{1}{2}} = \mathbf{u}_d^{n+\frac{1}{2}} - \mathbf{G}\varphi \tag{136}$$

The total velocity at face centers at half time steps is computed using

$$\mathbf{u}^{n+\frac{1}{2}} = \mathbf{u}_h + \mathbf{u}_d^{n+\frac{1}{2}} + \mathbf{u}_p^n \tag{137}$$

where the transverse components of $\mathbf{u}_h$ and $\mathbf{u}_p$ are computed by averaging the normal components in the same manner as the transverse gradient $\mathbf{G}$ is computed.

Computing $\mathbf{A_d u}$ and $div(\tilde{\rho}\mathbf{u})$

Now, we have all the terms that are needed to compute the advective terms

$$[div(\tilde{\rho}\mathbf{u})]_{ij}^{n+\frac{1}{2}} \approx \left[D\left(\tilde{\rho}^{n+\frac{1}{2}}\mathbf{u}^{n+\frac{1}{2}}\right)\right]_{ij} \tag{138}$$

$$\begin{aligned}[\mathbf{A_d u}]_{ij}^{n+\frac{1}{2}} \approx &\left[D\Big(\mathbf{u}^{n+\frac{1}{2}} \otimes \mathbf{u}_d^{n+\frac{1}{2}}\Big)\right]_{ij} + \left[D\Big(\mathbf{u}_d^{n+\frac{1}{2}} \otimes \Big(\mathbf{u}_p^n + \mathbf{u}_h\Big)\Big)\right]_{ij} \\ &-\mathbf{u}_{d,ij}^{n+\frac{1}{2}}\Big(D\mathbf{u}^{n+\frac{1}{2}}\Big)_{ij} - \Big(\mathbf{u}_p^n + \mathbf{u}_h\Big)_{ij}\Big(D\mathbf{u}_d^{n+\frac{1}{2}}\Big)_{ij}\end{aligned} \tag{139}$$

3.2 Discretization of the Operators on Cut Cells

An embedded boundary (EB) formulation is used to model the orography, *i.e* the mountain ranges. The mountain cuts cells as shown on Figure 4 and some faces are cut while some others are completely covered. The fact that some faces are not full faces has consequences on how we evaluate the operators presented in 3.1 and this section presents what is done differently on the embedded boundary. This approach follows Johansen and Colella [16] for elliptic problems. For hyperbolic problems, similar ideas have been used for incompressible Euler equations [2].

Gradient $\mathbf{G}$

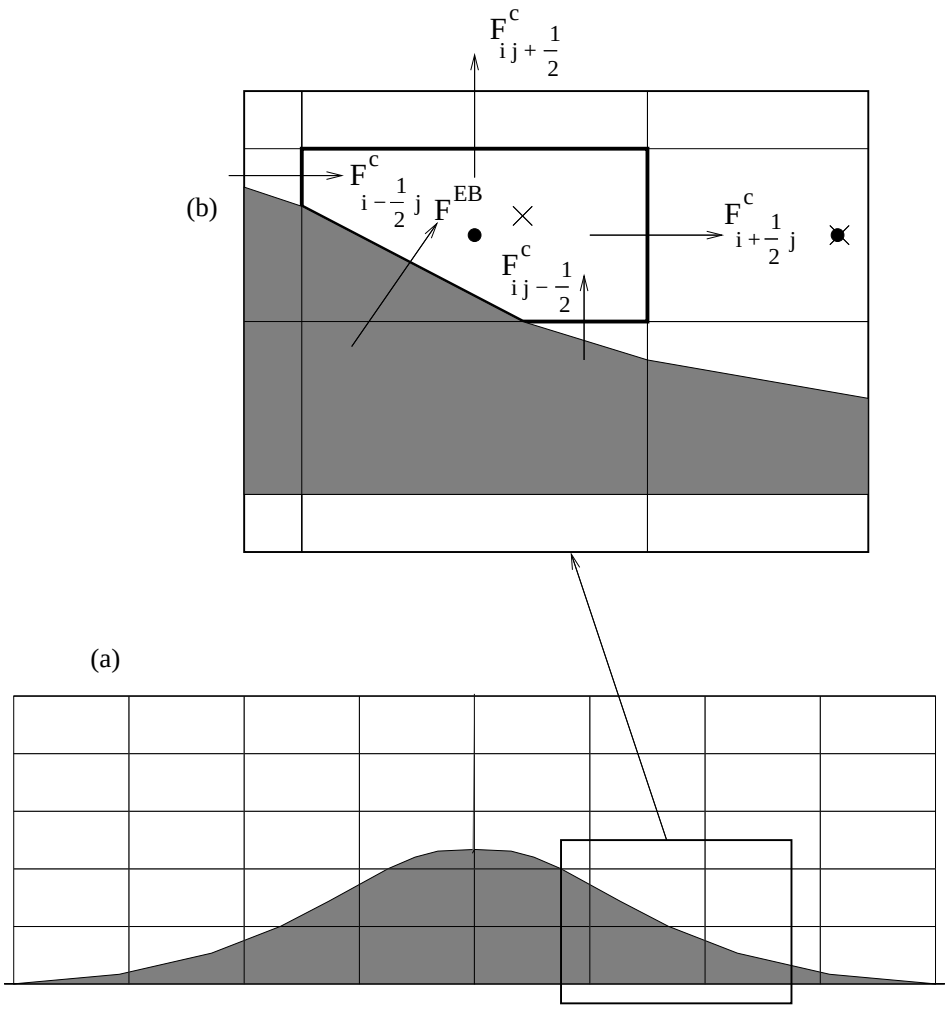

Fig. 4. Schematics of the embedded boundary with cut cells.

The gradient in the normal direction is unchanged. However, for the tangential gradient, we need the value of the normal gradient on four faces, some of which might not be available on irregular cells. The missing gradients are, then, extrapolated to second order as shown in Figure 5 and formula (111) remains unchanged.

Cell-Centered Gradient $\mathbf{G}_o$

In the average procedure, we need quantities at faces and, on some of the irregular cells, these quantities might not be available as a face might be covered. When one quantity is missing, we extrapolate to second order from the non-covered faces in the normal direction and then proceed to the arithmetic averaging as in (113).

Divergence D

When we had only regular cells, D ensured that we had a conservative dis-

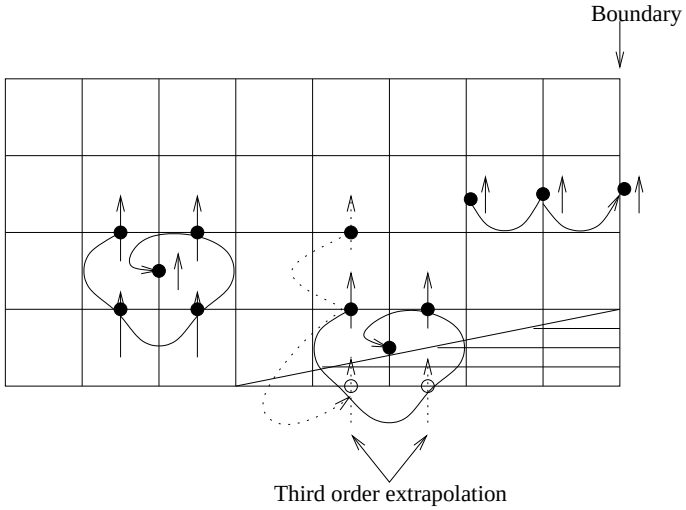

Fig. 5. Tangential gradient.

cretization of the divergence operator. However, if we used equation (115) when the cell is not regular, we would lose the conservative property.

To find the expression of the conservative divergence on cut cells, we average over the volume of the cell and then use Stokes' theorem to transform a volume integral into a surface integral so that we recover a flux balance

$$\nabla \cdot \mathbf{F}(\mathbf{u}) \approx \frac{1}{V} \int_V \nabla \cdot \mathbf{F} dV \tag{140}$$

$$\approx \frac{1}{V} \oint_S \mathbf{F} \cdot \mathbf{n} dS \tag{141}$$

$$\approx \frac{1}{\kappa_{ij}} \left[\frac{\alpha_{i+\frac{1}{2}j} F^c_{i+\frac{1}{2}j} - \alpha_{i-\frac{1}{2}j} F^c_{i-\frac{1}{2}j}}{\Delta x} + \frac{\alpha_{ij+\frac{1}{2}} F^c_{ij+\frac{1}{2}} - \alpha_{ij-\frac{1}{2}} F^c_{ij-\frac{1}{2}}}{\Delta x} + \alpha^{EB} F^{EB} \right] \tag{142}$$

where the superscript ^{c} represents quantities taken at the centroid of the faces, which may be different from the center of the face, and the superscript ^{EB} represents the quantities at the embedded boundary. $\alpha_{i+\frac{1}{2}j}$ is the area fraction of the face $(i + \frac{1}{2}j)$, defined as the ratio of the actual face area over the face area of the regular mesh spacing in this direction, and κ_{ij} is the volume fraction defined as the ratio of the volume of the cell over the volume of a regular rectangular cell. $\mathbf{F}_{i+\frac{1}{2}j}$ is the flux on face $(i+\frac{1}{2}j)$ and is illustrated on Figure 4(b).

Equation (142) gives an easy expression to compute the divergence of a flux on a cut-cell. Note that when the cell is regular, *i.e.* $\alpha = 1$, $\kappa = 1$ and

$\alpha^{EB} = 0$, we recover the classical expression for the divergence of a vector. This expression is however not sufficient as the volume fraction κ has the potential of becoming arbitrarily small, posing major accuracy and stability problems. When using the divergence operator to solve a Poisson's equation for example, multiplying both sides of the equation by κ removes the potential singularity. This approach is not possible for an explicit method.

Redistribution

When computing the advective terms in a complex PDE, we eliminate the κ in the denominator of (142) by using a mixed update of the form

$$\nabla \cdot \mathbf{F}(\mathbf{u}) = \kappa \nabla^C \cdot \mathbf{F}(\mathbf{u}) + (1-\kappa)\nabla^{NC} \cdot \mathbf{F}(\mathbf{u}) \tag{143}$$

where $\nabla^C \cdot \mathbf{F}$ is the conservative divergence as expressed in Equation (142) and $\nabla^{NC} \cdot \mathbf{F}$ is the non-conservative divergence that has the same expression as the divergence on regular rectangular cells, where the data is taken at face centers and extrapolated to covered faces if needed. This update (143) is not conservative, so we compute the mass δM that was added by using the non-conservative update

$$\delta M = \kappa \left[\nabla \cdot \mathbf{F}(\mathbf{u}) - \nabla^C \cdot \mathbf{F}(\mathbf{u})\right] \tag{144}$$

$$= \kappa(1-\kappa) \left[\nabla^{NC} \cdot \mathbf{F}(\mathbf{u}) - \nabla^C \cdot \mathbf{F}(\mathbf{u})\right] \tag{145}$$

and redistribute it to adjacent cells to ensure overall conservation of mass ([4], [6], [27]).

The complications arising from the presence of cut-cells are widely compensated by the advantages of having an underlying rectangular grid on the computational domain: the grid generation is stable and well-understood, and the coupling to structured AMR is straightforward.

Extrapolating to Covered Faces

To compute the non-conservative divergence in equation (143) that takes data on face centers, we need values on covered faces if there are any covered faces in the cut-cell. These values are extrapolated from adjacent faces and cells as pictured on Figure 6. For example, to extrapolate the quantity W on the covered face shown on Figure 6, we compute

$$\left(W^{n+\frac{1}{2}}_{i-\frac{1}{2},j}\right)^+_{\mathbf{A}} = W^n_{i+1,j} + \frac{1}{2}\left(-3 - \frac{\Delta t}{\Delta x} u^n_{i+1,j}\right)(\Delta_x W)^n_{i+1,j}$$

$$-\frac{\Delta t}{2\Delta z} w^n_{i+1j} \left[W\right]^n_{z,\, i+1j} - \frac{\Delta t}{2} R^n_{i+1j} \tag{146}$$

$$\left(W^{n+\frac{1}{2}}_{i-\frac{1}{2},j}\right)^+_{\mathbf{B}} = W^n_{i-1,j+1} + \frac{1}{2}\min\left\{\left(1 - \frac{\Delta t}{\Delta x} u^n_{i-1,j+1}\right), 1\right\}(\Delta_x W)^n_{i-1,j+1}$$
$$-(W^n_{i-1,j+2} - W^n_{i-1,j+1}) - \frac{\Delta t}{2\Delta z} w^n_{i-1j+1} \left[W\right]^n_{z,\, i-1j+1}$$
$$-\frac{\Delta t}{2} R^n_{i-1j+1} \tag{147}$$

where W satisfies an equation of the form

$$\frac{\partial W}{\partial t} + \mathbf{u}.\mathbf{grad}(W) + R(x,z,t) = 0 \tag{148}$$

The final density on the covered face is taken to be:

$$\left(W^{n+\frac{1}{2}}_{i-\frac{1}{2},j}\right)^{\pm} = n_x^2 \left(W^{n+\frac{1}{2}}_{i-\frac{1}{2},j}\right)^{\pm}_{\mathbf{A}} + n_z^2 \left(W^{n+\frac{1}{2}}_{i-\frac{1}{2},j}\right)^{\pm}_{\mathbf{B}} \tag{149}$$

where n_x and n_z are the components of the normal in the horizontal and vertical direction.

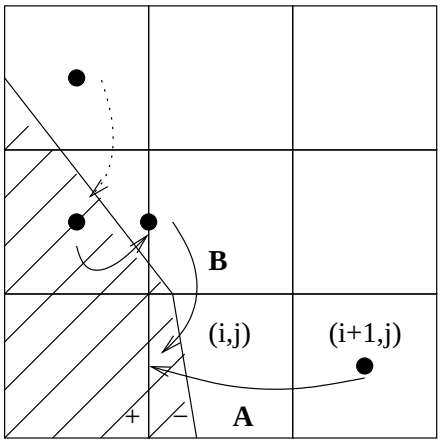

Fig. 6. Schematics of the extrapolation scheme to a covered face.

4 Results

4.1 Perturbational Gravity-Wave Test Problem

In the asymptotic analysis of section 1, we showed that we could extract a finite collection of discrete traveling gravity waves from the fully compressible

equations in the limit of low Mach and Froude numbers and small aspect ratio. The details of the derivation can be found in the Appendix.

We set up this example to verify the asymptotics results numerically, using the full compressible equations. The problem is initialized to be a traveling wave in the fastest mode and, following the asymptotic analysis, we expect to see the wave propagate and stay in the fastest mode.

4.1.1 Initialization

The pressure π_H and the solenoidal velocity are initialized as

$$\hat{u}_d(x, z, t = 0) = G(x) r^o(z) \tag{150}$$
$$\hat{\pi_H}(x, z, t = 0) = c^o \hat{u}_d(x, z, t = 0) \tag{151}$$

or identically for the pressure π_H

$$\pi_H(x, z, t = 0) = \rho_o c^o u_d(x, z, t = 0) \tag{152}$$

where r^o is the eigenvector associated with the fastest mode and c^o is the speed of the fastest wave. $G(x)$ is a Gaussian function

$$G(x) = \frac{\alpha}{\sqrt{2\pi}\sigma} exp\left(-\frac{(x - x_o)^2}{2\sigma^2}\right) \tag{153}$$

The remainder of the initialization must be done carefully to avoid artificially sending energy in modes that are not the fastest mode. First, the vertical component of the solenoidal velocity is initialized using the anelastic constraint (9)

$$w_d(x, z, t = 0) = \frac{1}{\eta_o} \int_0^z \eta_o \left(\frac{c^{o2}}{c_o^2} - 1\right) \frac{\partial u_d}{\partial x} dz \tag{154}$$

When computing the discrete integral, particular care needs to be taken to ensure that the discrete $\mathbf{u}_d$ satisfies the condition

$$D\eta_o \mathbf{u}_d = 0 \tag{155}$$

The potential velocity is then initialized using equation (66). We use the fact that $\mathbf{u}_p$ is a gradient

$$\mathbf{u}_p = \mathbf{grad}\varphi \tag{156}$$

and this yields

$$\mathbb{L}_{\frac{1}{\eta_o}}\varphi = -\frac{\eta_o}{\rho_o c_o^2}\frac{\partial \pi_H}{\partial t} \tag{157}$$

The time derivative of the pressure π_H is found by using the relationship derived in Appendix

$$\lambda^o \frac{\partial \hat{\pi}_H}{\partial t} + \frac{\partial \hat{u}_d}{\partial x} = 0 \tag{158}$$

since all the quantities are taken along the first eigenmode. φ then verifies

$$\mathbb{L}_{\frac{1}{\eta_o}}\varphi = -\eta_o \frac{c^{o2}}{c_o^2}\frac{\partial u_d}{\partial x} \tag{159}$$

The rest of the quantities are initialized according to their definitions.

4.1.2 Results

In this example, we use different domain sizes and different grid refinements to verify the asymptotics, as shown in Table 2

	$\varepsilon = 0.05$	$\varepsilon = 0.025$	$\varepsilon = 0.0125$	$\varepsilon = 0.00625$
Domain length (km)	256	512	1024	2048
Domain height (km)	12.8	12.8	12.8	12.8

Table 2
Different cases used for the asymptotic analysis.

Figures 7(a), (b) and (c) show that we obtain a traveling wave solution for aspect ratios of 0.025 and under. Figure 8 and 9(a) show that the decay in the amplitude of the solution and the amount of energy that gets transfered into the slow modes decrease as the aspect ratio decreases, as this means that the asymptotic assumptions are better verified. Figure 9(b) shows that the convergence is first order.

Figure 7(d) shows that we are not quite in the asymptotics regime for $\varepsilon = 0.05$. The traveling wave gets deformed at the beginning of the simulation on the

left of the propagating front and then this deformed wave propagates. The decay in amplitude as the wave propagates is much larger than in the cases where we are in the asymptotic regime, and a much larger part of the motion gets transferred from the fastest mode to the slow modes.

However, it is to be noted that even when the asymptotic assumptions hold loosely (as is the case with $\varepsilon = 0.05$), the percentage of the solution that gets transferred into the slow modes is under 4% for π_H and under 6% for u_d on a 128×64 grid. We also notice that the smaller ε is, the closer the propagation velocity is to c^o with a very good match for $\varepsilon = 0.0125$ as seen on Figure 8.

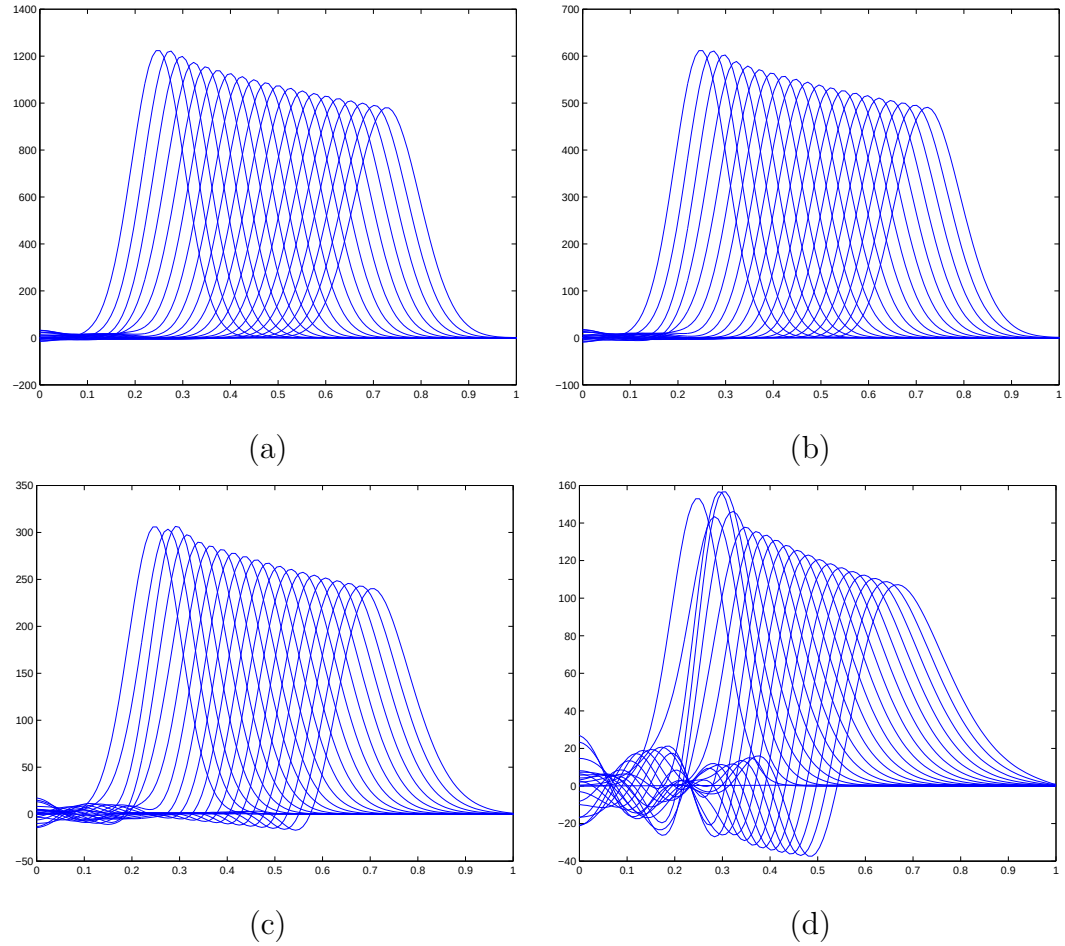

Fig. 7. π_H history on a 128×64 grid for different aspect ratios: (a) $\varepsilon = 0.00625$, (b) $\varepsilon = 0.0125$, (c) $\varepsilon = 0.025$, and (d) $\varepsilon = 0.05$.

4.2 Mountain Lee Waves

Our algorithm is now tested on the classical examples of gravity waves found in Durran ([10] and [12]). In these examples, a uniform wind with a speed of $20\,m/s$ passes over a $600\,m$, as pictured on Figure 10. The mountain has the

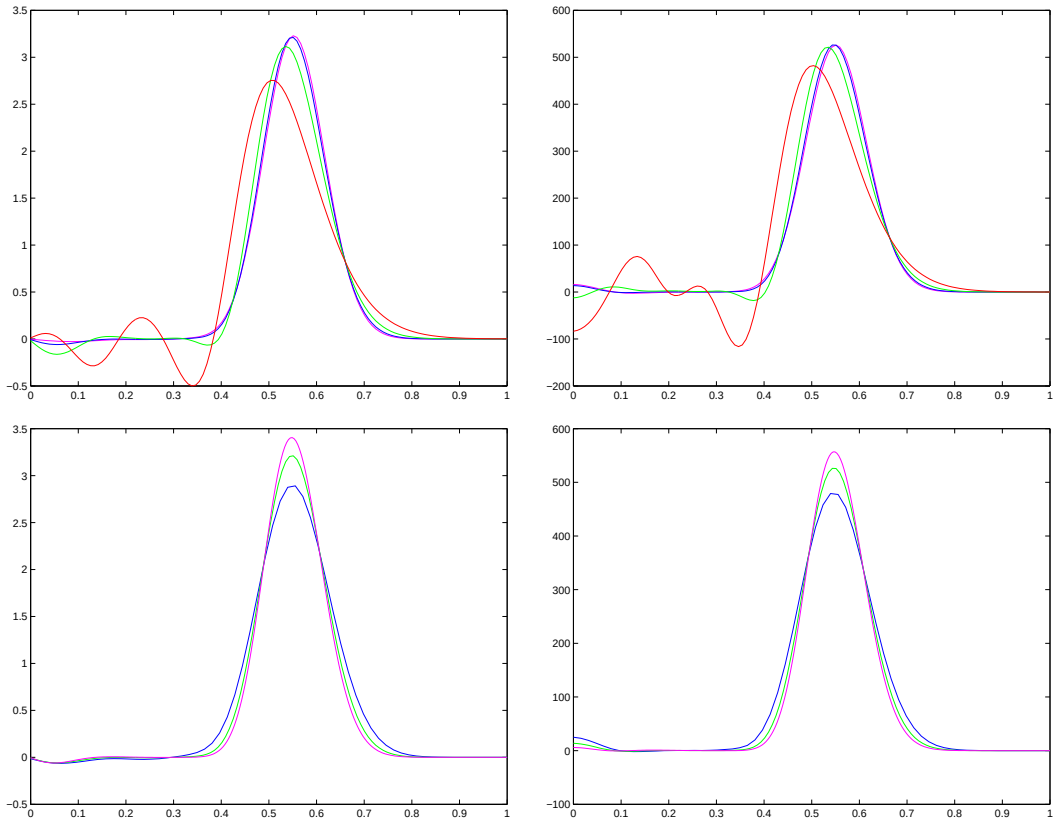

Fig. 8. u_d (left) and π_H (right), above for different aspect ratios holding the grid size fixed at 128×64: 0.05 (red), 0.025 (green), 0.0125 (blue), 0.00625 (pink); and below for different resolutions holding the aspect ratio fixed at 0.0125: 64×32 (blue), 128×64 (green), 256×128 (pink).

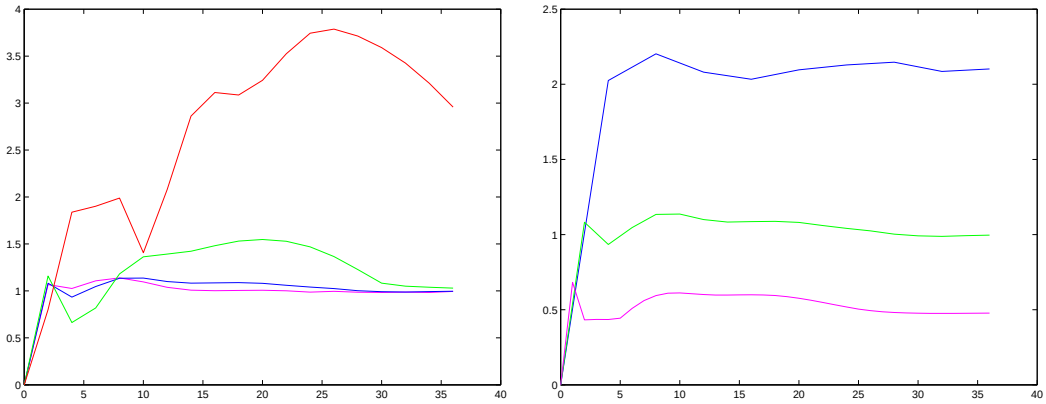

(a) (b)

Fig. 9. Percentage of the π_H solution that gets transfered from the fast mode to the slows modes; (a) for different aspect ratios holding the grid size fixed at 128×64: 0.05 (red), 0.025 (green), 0.0125 (blue), 0.00625 (pink), (b) for different grid resolutions holding the aspect ratio fixed at 0.0125: 64×32 (blue), 128×64 (green), 256×128 (pink)

shape of a "witch of Agnesi"

$$z_{Mountain}(x) = \frac{ha}{(x - x_o)^2 + a^2} \tag{160}$$

where $a = 10\,km$ is the mountain width, $h = 600\,m$ is the mountain height and $x_o = 72\,km$ is the position of the mountain crest.

The numerical domain measures $180\,km \times 12.8\,km$ and there is a $6.3\,km$ deep sponge layer on top of the domain and a $30\,km$ deep sponge layer on either side of the domain. The sponge layers damp the reflection of spurious gravity waves on the top and the sides of the domain.

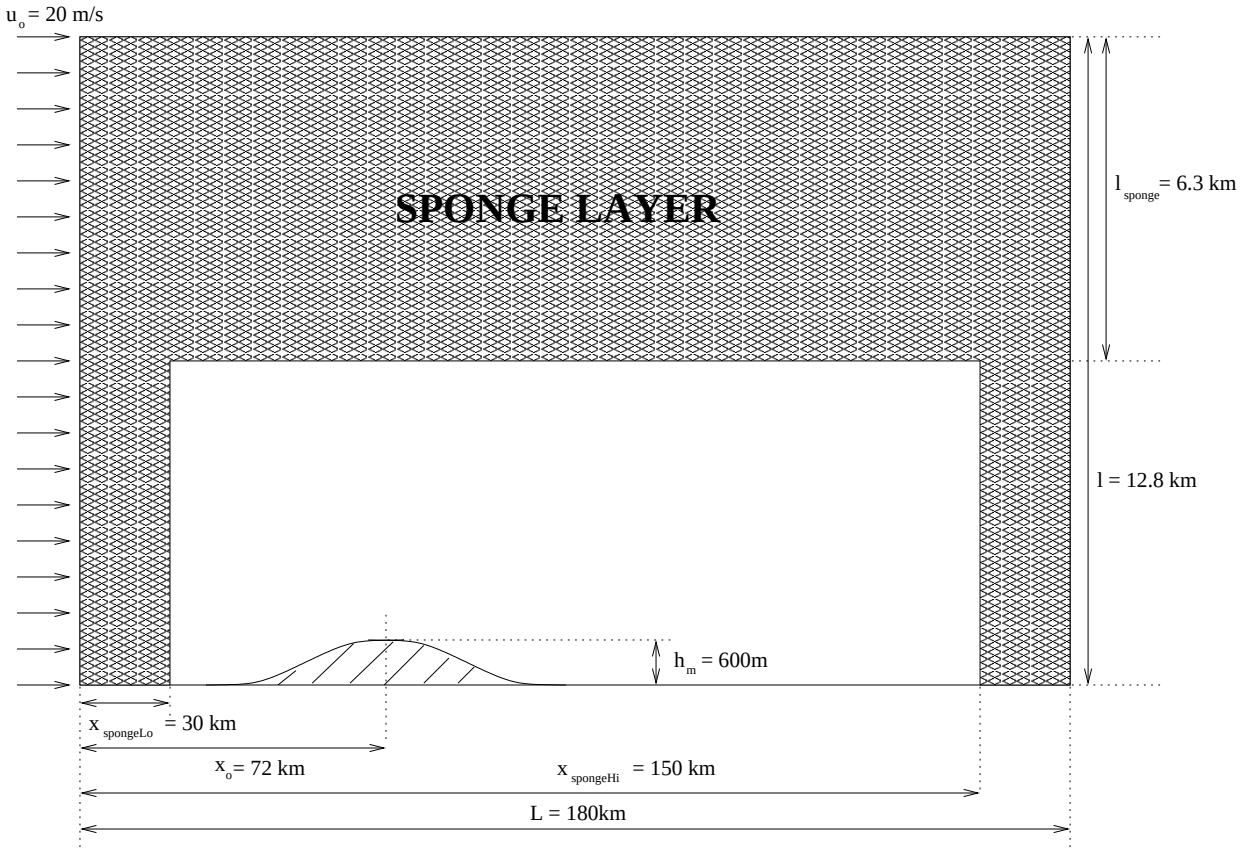

Fig. 10. Schematic of the parameters.

The atmosphere is a two-layered atmosphere and, in each layer, the Brunt-Väisälä frequency is a constant that takes one of these two values $0.01\,s^{-1}$ or $0.02\,s^{-1}$. The initial background density is given by

$$\rho_o(z) = \rho_{oi} \exp\left(-\frac{N_i^2(z - z_i)}{g}\right) \left(\frac{1 - (\gamma - 1)C_i \exp\left(-\frac{N_i^2 z}{g}\right)}{1 - (\gamma - 1)C_i \exp\left(-\frac{N_i^2 z_i}{g}\right)}\right)^{\left(\frac{1}{\gamma - 1}\right)} \tag{161}$$

where $i \in \{L, U\}$, $z_L = 0$, $z_U = H$ and the constants C_i are given by

$$C_L = -\frac{\frac{2\rho_o g^2}{\gamma p_o N_L^2}}{1 - (\gamma - 1)\frac{2\rho_o g^2}{\gamma p_o N_L^2}} \tag{162}$$

$$C_U = C_o \exp\left(-\frac{N_L^2 H}{g}\right)\left(\frac{N_L}{N_U}\right)^2 \frac{1}{1 - (\gamma - 1)C_L \exp\left(-\frac{N_L^2 H}{g}\right)} \tag{163}$$

The initial background pressure is then given by the hydrostatic relation (7).

According to linear theory, there are four possible tuned and detuned cases that can occur in a two-layered atmosphere, yielding gravity waves in some cases, depending on the position (top or bottom) of the layer with higher stability and on the value of the phase shift between the ground and the interface between the two layers. Table 3 presents a summary of the four possible cases. In Table 3, N_L is the Brunt-Väisälä frequency of the lower layer, N_U is the Brunt-Väisälä frequency of the upper layer and H is the height of the interface.

Case	N_L (s^{-1})	N_U (s^{-1})	H (m)	Amplitude of waves
(a)	0.02	0.01	1571	weak
(b)	0.02	0.01	3142	strong
(c)	0.01	0.02	3142	strong

Table 3
Position of the interface and wave response for different tuned and detuned cases.

Figure 11 represents cases (a), (b) and (c) shown in Table 3. Here, the grid spacing is 128×64 cells and the time step is $\Delta t = 15s$. The benchmark results from Durran were run using a small time step of $5s$ and a large time step of $10s$. Table 4 shows that the time step that we have chosen satisfies the CFL condition for the fastest gravity wave whose speed is computed using the analysis shown in Appendix.

	$N_L < N_U$		$N_U < N_L$
	quarter wavelength	half wavelength	quarter wavelength
c_{gw} (m/s)	74	80	59
Δt (s)	19.08	17.62	23.49

Table 4
Speed of fatest gravity wave c_{gw} and maximum time step for the lee-waves examples

Figure 11 compares qualitatively well with Figure 1 from Durran ([10]). For case (c), the match is remarkable and the positions of the crest of the waves

are almost identical. For cases (a) and (b), the match is also very good. The waves have the same wavelength than the one found in Durran, but their amplitudes differ slightly. For case (b), we also recover the main features of the isentropes: the amplitudes of the gravity waves increase with height while in the lower layer and decrease with height while in the upper layer, the sag starts at the crest of the mountain and ends near the foot of the mountain before the gravity waves start to form, and the sag is replaced by a big jump in the upper layer.

Case (b) is also run on a 256×128 grid with a time step of $\Delta t = 7.5\, s$ as shown in Figure 12. The wavelengths and the nominal position of the isentropes are identical for the finer and coarser resolution. However, for the finer resolution, the amplitudes of the gravity waves do not decay as fast away from the mountain as they do in Figure 11(b).

5 Conclusion

We developped a non-hydrostatic model that uses an embedded boundary method to represent mountain ranges. The numerical algorithm uses a splitting to separate the fast acoustic dynamics from the slower anelastic dynamics. In the limit of small Mach number and small aspect ratio, we recover the anelastic approximation, but we do not use the asymptotics in our formulation. The acoustic waves are treated implicitely while the advection is treated explicitely. Special attention is given to the spatial and time discretization, as well as the centering of the variables. Finally, we present a set of results that compares very well with the classical gravity waves results presented in Durran. We were able to obtain accurate results with a unique time step that is much larger than the one used in previous studies.

Acknowledgement

We would like to acknowledge Dr. Joseph Tribbia for suggesting that we look at the vertical normal mode analysis.

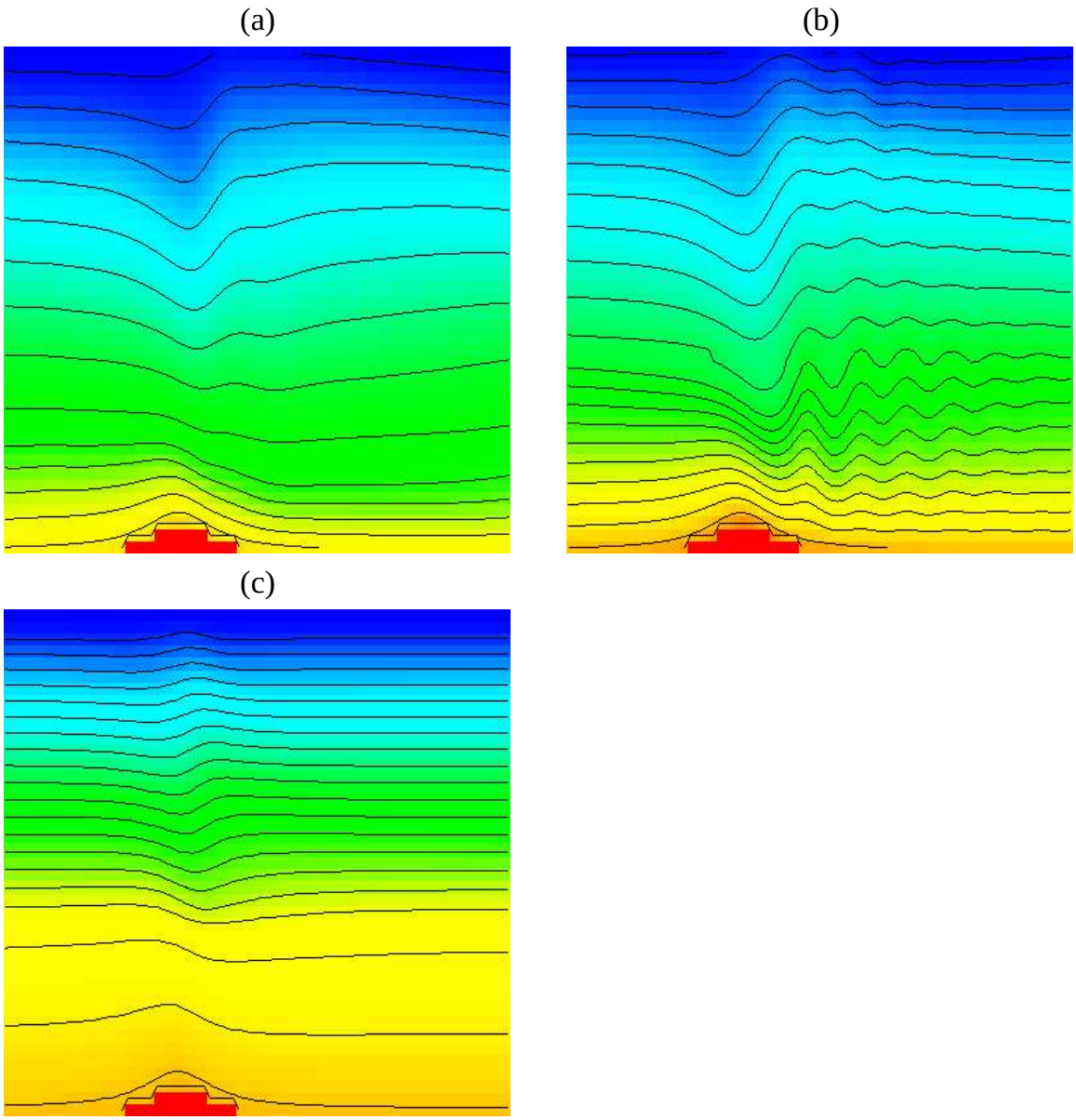

Fig. 11. Isentropes for a two-layered atmosphere flowing over a 600 m high mountain at $t = 10000\,s$. (a) Interface at 1571 m, one-quarter wavelength, (b) interface at 3141 m, one-half wavelength and (c) interface at 3141 m, one-quarter wavelength.

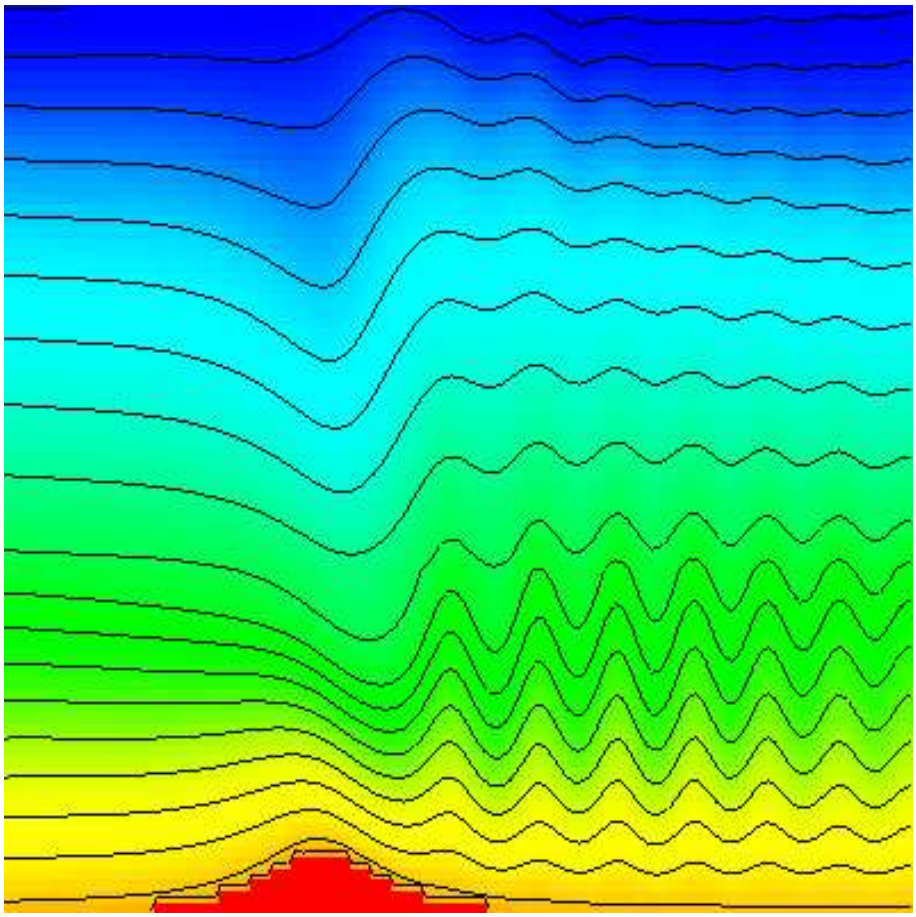

Fig. 12. Case (b) solved on a 256×128 grid

Appendix: Determination of the Time Step and of the Fastest Gravity Wave Speed

The splitting allows to isolate and treat implicitly acoustic waves. Therefore, the speed of the fastest gravity wave c_{gw} is now setting a constraint on the time step

$$\Delta t < \frac{\Delta x}{c_{gw}} \tag{164}$$

Gravity waves are horizontal traveling waves whose dynamics is mainly described by the solenoidal part of the flow, that is equations (20) and (21) that can be rewritten

$$\frac{\partial \tilde{\rho}}{\partial t} + \rho_o w \left[\frac{1}{\rho_o} \frac{d\rho_o}{dz} - \frac{1}{\eta_o} \frac{d\eta_o}{dz} \right] = -div(\tilde{\rho}\mathbf{u}) - \frac{\rho_o}{\eta_o} div(\eta_o \mathbf{u}_p) \tag{165}$$

$$\frac{\partial u_d}{\partial t} + \frac{1}{\rho} \frac{\partial \pi_H}{\partial x} = -\left(\mathbf{A}_d \mathbf{u}\right)_x - \frac{1}{\rho} \frac{\partial \pi_I}{\partial x} - \left[\mathbb{P}_o \left(\frac{1}{\rho} \mathbf{grad}\delta + \mathbf{grad} \frac{|\mathbf{u}_p + \mathbf{u}_h|^2}{2} \right) \right]_x \tag{166}$$

We want the right-hand sides of equations (165) and (166) to be small so that we can recover the classical system of equations for traveling waves. Analyzing the orders of magnitude of the different terms shows that $\frac{\rho_o}{\eta_o} div(\eta_o \mathbf{u}_p)$ is the dominant term in equation (165) and that, from equation (23), $\frac{\rho_o}{\eta_o} div(\eta_o \mathbf{u}_p) + \frac{1}{c_o^2} \frac{\partial \pi_H}{\partial t}$ is small. Therefore, we subtract $\frac{1}{c_o^2} \frac{\partial \pi_H}{\partial t}$ to both sides of equation (165)

$$\frac{\partial \tilde{\rho}}{\partial t} - \frac{1}{c_o^2} \frac{\partial \pi_H}{\partial t} + w\rho_o \left[\frac{1}{\rho_o} \frac{d\rho_o}{dz} - \frac{1}{\gamma p_o} \frac{dp_o}{dz} \right] = -div(\tilde{\rho}\mathbf{u}) - \left(\frac{\rho_o}{\eta_o} div(\eta_o \mathbf{u}_p) + \frac{1}{c_o^2} \frac{\partial \pi_H}{\partial t} \right) \tag{167}$$

$$\frac{\partial u_d}{\partial t} + \frac{1}{\rho} \frac{\partial \pi_H}{\partial x} = -\left(\mathbf{A}_d \mathbf{u}\right)_x - \frac{1}{\rho} \frac{\partial \pi_I}{\partial x} - \left[\mathbb{P}_o \left(\frac{1}{\rho} \mathbf{grad}\delta + \mathbf{grad} \frac{|\mathbf{u}_p + \mathbf{u}_h|^2}{2} \right) \right]_x \tag{168}$$

Using equations (25) and (33) along with the definition of the Brunt Väisälä frequency $N = \sqrt{-g \left[\frac{1}{\rho_o} \frac{d\rho_o}{dz} - \frac{1}{\gamma p_o} \frac{dp_o}{dz} \right]}$, we obtain

$$
\begin{aligned}
-\frac{\eta_o g}{\rho_o N^2}\left(\frac{1}{g}\frac{\partial}{\partial z}+\frac{1}{c_o^2}\right)\frac{\partial \pi_H}{\partial t}-\eta_o w &= R^*_{\pi_H} \\
&= -\frac{\eta_o g}{\rho_o N^2} div(\tilde{\rho}\mathbf{u}) - \frac{\eta_o g}{\rho_o N^2}\left(\frac{\rho_o}{\eta_o} div(\eta_o \mathbf{u}_p) + \frac{1}{c_o^2}\frac{\partial \pi_H}{\partial t}\right)
\end{aligned} \tag{169}
$$

$$
\begin{aligned}
\frac{\partial u}{\partial t}+\frac{1}{\rho_o}\frac{\partial \pi_H}{\partial x} &= R_u \\
&= -\left(\mathbf{A}_d \mathbf{u}\right)_x - \frac{1}{\rho}\frac{\partial \pi_I}{\partial x} - \left(\frac{1}{\rho}-\frac{1}{\rho_o}\right)\frac{\partial \pi_H}{\partial x} \\
&\quad - \left[\frac{1}{\rho}\frac{\partial \delta}{\partial x} + \frac{\partial}{\partial x}\left(\frac{|\mathbf{u}_p+\mathbf{u}_h|^2}{2}\right)\right]
\end{aligned} \tag{170}
$$

Formal linear analysis shows that the two right hand-side terms $R^*_{\pi_H}$ and R_u are either quadratic in the perturbations or small because either the Mach number or the Froude number is small.

The idea is now to obtain a wave equation with variables x and t while averaging continously the vertical variable z. First, differentiate equation (169) with respect to z

$$
\begin{aligned}
\mathcal{L}_z \frac{\partial \pi_H}{\partial t}+\frac{\partial \eta_o u_d}{\partial x} &= R_{\pi_H} \\
&= -\frac{\partial}{\partial z}\left\{\frac{\eta_o g}{\rho_o N^2}\left[div(\tilde{\rho}u)+\frac{1}{c_0^2}\frac{\partial \pi_H}{\partial t}\right]+\frac{g}{N^2}div(\eta_0 \mathbf{u}_p)\right\} \\
&\quad + div(\eta_o \mathbf{u}_p) + \frac{\eta_o}{\rho_o c_o^2}\frac{\partial \pi_H}{\partial t} - \frac{\partial \eta_o u_p}{\partial x}
\end{aligned} \tag{171}
$$

$$
\begin{aligned}
\frac{\partial u_d}{\partial t}+\frac{1}{\rho_o}\frac{\partial \pi_H}{\partial x} &= R_u \\
&= -\left((\mathbf{A}_d \mathbf{u})_x + \frac{1}{\rho}\frac{\partial \pi_I}{\partial x} + \left(\frac{1}{\rho}-\frac{1}{\rho_o}\right)\frac{\partial \pi_H}{\partial x} + \frac{\partial u_p}{\partial t}\right. \\
&\quad \left. + \left[\frac{1}{\rho}\frac{\partial \delta}{\partial x} + \frac{\partial}{\partial x}\left(\frac{|\mathbf{u}_p+\mathbf{u}_h|^2}{2}\right)\right]\right)
\end{aligned} \tag{172}
$$

where we have added $\dfrac{\eta_o}{\rho_o c_o^2}\dfrac{\partial \pi_H}{\partial t}$ to both sides of equation (171) and used

$$
\frac{\partial \eta_o w}{\partial z}+\frac{\partial \eta_o u}{\partial x} = div(\eta_o \mathbf{u}_p) \tag{173}
$$

and where

$$\mathcal{L}_z = -\frac{\partial}{\partial z}\left[\frac{\eta_o g}{\rho_o N^2}\left(\frac{1}{g}\frac{\partial}{\partial z}+\frac{1}{c_o^2}\right)\right]+\frac{\eta_o}{\rho_o c_o^2} = -\xi\left[\frac{\partial}{\partial z}\zeta\frac{\partial}{\partial z}+\chi\right] \tag{174}$$

with

$$\xi = exp\left(-\int_o^z \frac{g}{c_o^2}dz\right) \tag{175}$$

$$\zeta = \frac{\eta_o}{\rho_o N^2} exp\left(\int_o^z \frac{g}{c_o^2}dz\right) \tag{176}$$

$$\chi = \frac{\eta_o}{\rho_o c_o^2}\left[(\gamma-1)\frac{g^2}{N^2 c_o^2}-1\right] exp\left(\int_o^z \frac{g}{c_o^2}dz\right) \tag{177}$$

Introduce the following change of variables

$$\hat{\pi}_H = \sqrt{\frac{\eta_o}{\rho_o \xi}}\pi_H \tag{178}$$

$$\hat{u}_d = \sqrt{\frac{\rho_o \eta_o}{\xi}}u_d \tag{179}$$

$$\hat{\mathcal{L}}_z = \sqrt{\frac{\rho_o}{\eta_o \xi}}\mathcal{L}_z\sqrt{\frac{\rho_o \xi}{\eta_o}} \tag{180}$$

$$\hat{R}_{\pi_H} = \sqrt{\frac{\rho_o}{\eta_o \xi}}R_{\pi_H} \tag{181}$$

$$\hat{R}_u = \sqrt{\frac{\rho_o \eta_o}{\xi}}R_u \tag{182}$$

and equations (169) and (170) become

$$\begin{aligned}\hat{\mathcal{L}}_z\frac{\partial \hat{\pi}_H}{\partial t}+\frac{\partial \hat{u}_d}{\partial x} &= \hat{R}_{\pi_H} \\ &= -\sqrt{\frac{\rho_o}{\eta_o \xi}}\frac{\partial}{\partial z}\left\{\frac{\eta_o g}{\rho_o N^2}\left[div(\tilde{\rho}\mathbf{u})+\frac{1}{c_o^2}\frac{\partial \pi_H}{\partial t}\right]+\frac{g}{N^2}div(\eta_o \mathbf{u}_p)\right\} \\ &\quad +\sqrt{\frac{\rho_o}{\eta_o \xi}}\left[div(\eta_o \mathbf{u}_p)+\frac{1}{c_o^2}\frac{\partial \pi_H}{\partial t}-\frac{\partial \eta_o u_p}{\partial x}\right]\end{aligned} \tag{183}$$

$$\begin{aligned}\frac{\partial \hat{u}_d}{\partial t}+\frac{\partial \hat{\pi}_H}{\partial x} &= \hat{R}_u \\ &= -\sqrt{\frac{\eta_o \rho_o}{\xi}}\left\{(\mathbf{A}_d\mathbf{u})_x+\frac{1}{\rho}\frac{\partial \pi_I}{\partial x}+\left(\frac{1}{\rho}-\frac{1}{\rho_o}\right)\frac{\partial \pi_H}{\partial x}\right.\end{aligned}$$

$$+\frac{1}{\rho}\frac{\partial \delta}{\partial x}+\frac{\partial}{\partial x}\left(\frac{|\mathbf{u}_p+\mathbf{u}_h|^2}{2}\right)-\frac{\partial u_p}{\partial t}\Bigg\} \tag{184}$$

Let λ^k and r^k, $k=1\dots N$, be the eigenvalues and eigenvectors of the discretized operator $\hat{\mathcal{L}}_z$. $\hat{\pi}_H$ and $\hat{u}$ can be decomposed on the orthonormal basis formed by the eigenvectors r^k

$$\hat{\pi}_H(x,z,t)=\sum_{k=1}^{N}\hat{\pi}_H^k(x,t)r^k(z) \tag{185}$$

$$\hat{u}_d(x,z,t)=\sum_{k=1}^{N}\hat{u}_d^k(x,t)r^k(z) \tag{186}$$

with

$$\hat{\pi}_H^k(x,t)=\int_0^{L_{top}}\hat{\pi}_H(x,z,t)r^k(z)dz \tag{187}$$

$$\hat{u}_d^k(x,t)=\int_0^{L_{top}}\hat{u}_d(x,z,t)r^k(z)dz \tag{188}$$

System (183)–(184) can then be rewritten after projection on the eigenvector r^k

$$\lambda^k\frac{\partial\hat{\pi}_H^k}{\partial t}+\frac{\partial\hat{u}_d^k}{\partial x}=\hat{R}_{\pi_H}^k \tag{189}$$

$$\frac{\partial\hat{u}_d^k}{\partial t}+\frac{\partial\hat{\pi}_H^k}{\partial x}=\hat{R}_u^k \tag{190}$$

The system of equations (189) and (190) is hyperbolic with wave speed $c_{gw}^k=\dfrac{1}{\sqrt{\lambda^k}}$. The wave speed c_{gw}^k is the speed of the gravity waves on the k^{th} mode and the fastest gravity wave with speed c_{gw} is constraining the time step.

References

[1] http://www.vets.ucar.edu/vg/CCM3T170/index.shtml

[2] Almgren A., Bell J., Colella P. and Marthaler T., "A Cartesian Grid Projection Method for the Incompressible Euler Equations in Complex Geometries", SIAM J. Sci. Comp., 18:5, Sept. 1997.

[3] Baer F. and Tribbia J.J. "On Complete Filtering of Gravity Modes through Nonlinear Initialization", *Monthly Weather Review*, **105**, pp.1536–1539, 1977.

[4] Bell J., Colella P. and Welcome M., "Conservative Front-Tracking for Inviscid Compressible Flow", in Proc. 10^{th} AIAA Computational Fluid Dynamics Conference, Honolulu, HI, pp. 814–822, 1991.

[5] Brannon P., "On the Anelastic Approximation for a Compressible Atmosphere", *Journal of the Atmospheric Sciences*, **53**(23), pp. 3618–3628, 1996.

[6] Chern I. and Colella P., "A Conservative Front-Tracking Method For Hyperbolic Conservation Laws", UCRL-97200 LLNL, 1987.

[7] Clark T., "A Small-Scale Dynamic Model Using a Terrain-Following Coordinate Transformation", *Journal of Computational Physics*, **24**, pp. 187–214, 1977.

[8] Colella P., Graves D. and Modiano D., "A Second-Order Embedded Boundary Method for Hyperbolic Conservation Laws", *Journal of Computational Physics*, (to be submitted).

[9] Colella P. and Pao K., "A Projection Method for Low Speed Flows", *Journal of Computational Physics*, **149**(2), pp. 245-269, 1999.

[10] Durran D., "Another Look At Downslope Windstorms. Part I: The Development of Analogs to Supercritical Flow in an Infinitely Deep, Continuously Stratified Fluid", *Journal of the Atmospheric Sciences*, **43**(21), pp.2527–2543, 1986.

[11] Durran D., "Improving the Anelastic Approximation", *Journal of the Atmospheric Sciences*, **46**(11), pp.1453–1461, 1989.

[12] Durran D., "Atmospheric Processes over Complex Terrain", *Meteorological Monographs*, **23**(45), pp.59–81, 1990.

[13] Durran D. and Klemp J.B., "A Compressible Model for the Simulation of Moist Mountain Waves", *Monthly Weather Review*, **111**, pp.2341–2360, 1983.

[14] Huang C.-Y., "A Forward-in-Time Anelastic Nonhydrostatic Model in a Terrain Following Coordinates", *Monthly Weather Review*, **128**, pp. 2108–2134, 2000.

[15] Hubbard M.E. and Nikiforakis N., "A Three-Dimensional, Adaptive, Godunox-Type Model for Global Atmospheric Flows", *Monthly Weather Review*, **131**, pp. 1848–1864, 2003.

[16] Johansen H. and Colella P., "A Cartesian Grid Embedded Boundary Method for Poisson's Equation on Irregular Domains", *J. Comput. Physics*, **147**(1), pp. 60-85, 1998.

[17] Kato T. and Saito K., "Hydrostatic and Non-Hydrostatic Simulations of Moist Convection: Applicability of the Hydrostatic Approximation to a High-Resolution Model", *Journal of the Meteorological Society of Japan*, **73**(1), pp. 59–77, 1995.

[18] Klein R., "Asymptotic Analyses for Atmospheric Flows and the Construction of Asymptotically Adaptive Numerical Methods", *ZAMM*, **80**, pp. 765–777, 2000.

[19] Klemp . and Lilly D., "Numerical Simulation of Hydrostatic Mountain Waves", *Journal of the Atmospheric Sciences*, **35**, pp. 78–107, 1978.

[20] Kluzek E.B., Olson J. , Rosinski J.M., Truesdale J.E. and Vertenstein M., "User Guide to NCAR CCM3.6", Climate and Global Dynamics Division, National Center for Atmospheric Research, Boulder, CO.

[21] Keller T., "Implications of the Hydrostatic Assumption on Atmospheric Gravity Waves", *Journal of the Atmospheric Sciences*, **51**(13), pp. 1915–1929, 1994.

[22] Kim Y.-J. and Arakawa A., "Improvement of Orographic Gravity Waves Parametrization Using a Mesoscale Gravity Wave Model", *Journal of the Atmospheric Sciences*, **52**(11), pp. 1875–1902, 1995.

[23] Lilly D., "A comparison of incompressible, anelastic and Boussinesq Dynamics", *Atmospheric Research*, **40**, pp. 143–151, 1996.

[24] McCorquodale P., Colella P. and Johansen H., "A Cartesian Grid Embedded Boundary Method for the Heat Equation on Irregular Domains", *J. Comput. Physics*, **173**, pp. 620–635, 2001.

[25] Oliger J. and Sundstrom A., "Theoretical and practical aspects of some initial boundary-value problems in fluid dynamics", *SIAM Journal of Applied Mathematics*, **35**, pp. 419–446, 1978.

[26] Peltier W. and Clark T., "The Evolution and Stability of Finite-Amplitude Mountain Waves. Part II: Surface Wave Drag and Severe Downslope Windstorms", *Journal of the Atmospheric Sciences*, **36**, pp. 1498–1529, 1979.

[27] Pember R., Bell J., Colella P., Crutchfield W., Welcome M., "An Adaptive Cartesian Grid Method for Unsteady Compressible Flow in Irregular Regions", *Journal of Computational Physics*, **120**(2), pp. 278-304, 1995.

[28] Randall D., "The Anelastic and Boussinesq Approximations", unpublished (http://kiwi.atmos.colostate.edu:16080/group/dave/drweb/AneBous.pdf), 2000.

[29] Saito K., "A Numerical Study of the Local Downslope Wind "Yamaji-kaze" in Japan - Part 3: Numerical Simulation of the 27 September 1991 Windstorm with a Non-Hydrostatic Multi-Nested Model", *Journal of the Meteorological Society of Japan*, **72**(2), pp. 301–328, 1994.

[30] Temperton C., Williamson D.L. "Normal Mode Initialization for a Multilevel Grid-Point Model. Part I: Linear Aspects", *Monthly Weather Review*, **109**, pp.729–743, 1981.

[31] Tribbia J.J. "A Simple Scheme for High-Order Nonlinear Normal Mode Initialization", *Monthly Weather Review*, **112**, pp.278–284, 1984.

[32] Williamson D.L., Temperton C. "Normal Mode Initialization for a Multilevel Grid-Point Model. Part I: Nonlinear Aspects", *Monthly Weather Review*, **109**, pp.744–7757, 1981.